

# An adaptive coupling strategy for joint inversions that use petrophysical information as constraints

Björn Heincke[a], Marion Jegen[b], Max Moorkamp[c], Richard W. Hobbs[d], Jin Chen[b]

<sup>a</sup>*GEUS — Geological Survey of Denmark and Greenland,  
Øster Voldgade 10,  
DK-1350 Copenhagen, Denmark*

*E-mail (corresponding author): bhm@geus.dk*

<sup>b</sup>*GEOMAR — Helmholtz Centre for Ocean Research,  
Wischhofstrasse 1-3,*

<sup>c</sup>*University of Leicester,*

*Department of Geology,  
Leicester LE1 7RH, United Kingdom*

<sup>d</sup>*University of Durham,*

*Department of Earth Sciences,  
Durham DH1 3LE, United Kingdom*

---

## Abstract

Joint inversion strategies for geophysical data have become increasingly popular **as they allow for the efficient combination of** complementary information from different data sets. The algorithm used for the joint inversion needs to be flexible in its description of the subsurface so as to be able to handle the diverse nature of the data. Hence, joint inversion schemes are needed that 1) adequately balance data from the different methods, 2) have stable convergence behavior, 3) consider the different resolution power of the methods **used** and 4) link the parameter models in a way that they are suited for a wide range of applications.

Here, we combine **active source** seismic **P-wave** tomography, gravity and magnetotelluric (MT) data in a petrophysical joint inversion that accounts

for these issues. Data from the different methods are inverted separately and are linked through **constraints** accounting for parameter relationships. An advantage of performing the inversions separately is that no relative weighting between the data sets is required. To avoid perturbing the convergence behavior of the inversions by the coupling, the strengths of the constraints are readjusted at each iteration. The criterion we use to control the adaption of the coupling strengths is based on **variations in the** objective functions from the individual inversions. Adaption of the coupling strengths makes the joint inversion scheme then also applicable to subsurface conditions, where assumed relationships are not valid everywhere, because the individual inversions decouple if it is not possible to reach adequately low data misfits for the made assumptions. The coupling constraints depend on the relative resolutions of the methods, which leads to an improved convergence behavior of the joint inversion compared to a setup, where the resolution is not considered.

Another benefit of the proposed scheme is that structural information can easily be incorporated in the petrophysical joint inversion (no additional terms are added in the objective functions) by using mutually controlled structural weights for the smoothing constraints.

We test our scheme using data generated from a synthetic 2-D sub-basalt model. We observe that the adaption of the coupling strengths makes the convergence of the inversions very robust (data misfits of all methods are close to the target misfits) and that final results are always close to the true models independent of the parameter choices. Finally, the scheme is applied on real data sets from the Faroe-Shetland Basin to image a basaltic sequence

and underlying structures. The presence of a borehole and a 3-D reflection seismic survey in this region allows direct comparison and, hence, evaluate the quality of the joint inversion results. The results from joint inversion are more consistent with results from other studies than the ones from the corresponding individual inversions and the shape of the basaltic sequence is better resolved. However, due to the limited resolution of the individual methods used it was not possible to resolve structures underneath the basalt in detail, **indicating** that additional geophysical information (e.g. CSEM, reflection onsets) needs to be included.

*Keywords:* Joint inversion, adaptive coupling, sub-basalt imaging

---

## 1. Introduction

Joint inversions are integrated procedures that simultaneously invert data from different geophysical methods. They **have** become popular in the past decade and there are recent publications about joint inversions in many fields (see Moorkamp et al. (2016) for an overview). Compared to individual inversion of the same datasets resolutions are generally improved and the ambiguities reduced, if the parameters are linked with each other during the inversion stage. The resultant models from joint inversion typically have parameter distributions that are closer to the real distributions of the physical properties in the subsurface, which facilitates subsequent interpretation. However, there are number of problems in joint inversion algorithms; in particular if the involved methods are sensitive to different physical properties (e.g. seismic velocity, density and/or resistivity). This is because:

1. data sets from the individual methods consist of different data types,

15 sensitivity and numbers of measurements, so their influence on the final  
16 model have to be properly balanced during the joint inversion proce-  
17 dure. To find such optimum relative scaling can be difficult and im-  
18 proper scaling results in data from some methods being well-fitted, but  
19 data from other methods being seriously under-fitted (or over-fitted);

20 2. convergence behaviour is often complex and strongly non-linear for  
21 some methods (e.g. magnetotelluric, control source electromagnetic,  
22 seismic full-waveform tomography) and the convergence path through  
23 the model space of each method is typically different. The convergence  
24 behaviour and path is further complicated by the coupling within joint  
25 inversion. Hence, the joint inversion may get trapped in local minimum  
26 far away from an adequate solution where all methods have reasonable  
27 data misfits;

28 3. resolution capabilities of the methods differ and usually vary signifi-  
29 cantly with location in the model. Like the balance problem in (1)  
30 above, ignoring these resolution issues in the joint inversion algorithm  
31 may result in a bad data fit for some of the methods, some bias in the  
32 models or slow convergence behaviour;

33 4. assumptions used to link the different methods (or models), typically  
34 involve some approximations of the petrophysical or structural rela-  
35 tionships that are often not valid for the entire subsurface under in-  
36 vestigation. Too rigid implementation of these links or an improper  
37 choice of assumptions can result in serious and unpredictable errors in  
38 the joint inversion results.

39 For deterministic approaches that are **suitable for handling** large num-  
40 ber of unknowns and are applicable for problems with time consuming for-  
41 ward calculations, several strategies exist to deal with these problems. To  
42 find adequate relative scaling between the data sets (1st problem), most  
43 joint inversions algorithms consider only weighting that is defined by the  
44 assumed errors of the individual measurements (expressed by the data co-  
45 variance matrix). Other approaches are purely data driven (e.g. Xu, 2009)  
46 or use of multiplicative objective functions to balance the different data sets  
47 (e.g. Abubakar et al., 2009). Some inversion approaches (e.g. Günther and  
48 Rücker, 2006; Paasche and Tronicke, 2007; Bouchedda et al., 2012; Zhu and  
49 Harris, 2015) **attempt to overcome this problem** by independently inverting  
50 the data from different methods and share information from the parameter  
51 models between the different inversion runs to promote a similarity between  
52 the final models. Such joint inversions are commonly named "cooperative"  
53 and have the advantage that no relative weighting between the data sets is  
54 required.

55 To ensure convergence in deterministic inversions (2nd problem), sev-  
56 eral strategies are proposed that adjust the regularisation strength (Kilmer  
57 and O'Leary, 2001; Vogel, 2002) by applying e.g. L-curve fitting (Hansen,  
58 1993), generalized cross-validation (GCV) (Golub and Van Loan, 1996) or  
59 the discrepancy principle (Morozov, 1966; Vogel, 2002). For joint inversion  
60 e.g. Lelièvre et al. (2012) use a gradually decreasing regularisation that is  
61 determined at every iteration from the relationship between the actual data  
62 misfit and the specified target misfit. Other joint inversion approaches em-  
63 ploy Lagrange multipliers for balancing the coupling constraints that result

64 in a more stable convergence (e.g. Gallardo and Meju, 2004; Gallardo, 2007).

65 The impact of resolution power of the individual methods (3rd problem)  
66 can be handled by adjusting cell sizes (Lien, 2013) in the parameter models  
67 or using independent and spatially flexible regularization strengths for each  
68 parameter model.

69 Structural approaches, which assume that spatial variations in the dif-  
70 ferent parameter models are present at the same locations and are simi-  
71 larly orientated in space, are considered as valid for many subsurface condi-  
72 tions (4th problem) and are widely used (e.g. Haber and Oldenburg, 1997;  
73 Gallardo and Meju, 2004; Günther and Rücker, 2006; Doetsch et al., 2010;  
74 Molodtsov et al., 2013; Zhu and Harris, 2015). However, there are contri-  
75 butions (e.g. Lelièvre et al., 2012) that note that structural links provide  
76 a rather weak coupling resulting only in clear improvements compared to  
77 individual inversions in regions that are already relatively well-resolved by  
78 most of the individual methods; although other publications (e.g. Moorkamp  
79 et al., 2013) show that structural joint inversions can provide superior re-  
80 sults even in cases when low-resolution methods are involved. In contrast,  
81 other assumptions that are more rigorous and less generally valid, e.g. petro-  
82 physical coupling using parameter relationships (Lees and VanDecar, 1991;  
83 Afnimar et al., 2002; Moorkamp et al., 2011), often impose a strong cou-  
84 pling and result in significant improvement even for low resolution methods  
85 or in parts of the investigated subsurface volume that are not sampled by  
86 all of the methods. Which methods work best for a particular joint inver-  
87 sion problem needs to be determined on a case by case basis dependent on  
88 the survey design and the geological settings. Some approaches (Colombo

89 and Stefano, 2007; Lelièvre et al., 2010) have developed options to combine  
90 both structural and petrophysical information in the joint inversion. Other  
91 joint inversions either use more generally valid assumptions for petrophysical  
92 coupling by employing flexible parameter relationships that can be modified  
93 during the inversion process (Nielsen and Jacobsen, 2000; Lelièvre et al.,  
94 2012) or use approaches that invert directly for reservoir and rock proper-  
95 ties (e.g. Hoversten et al., 2006; Dell’Aversana et al., 2011). An alternative  
96 way of considering structural information is to use sharp-boundaries in joint  
97 inversions (e.g. Juhojuntti and Kamm, 2015) that allow strong contrasts at  
98 interfaces, but inherently assume that the subsurface consists of a number of  
99 distinct layers, an assumption that is not necessarily true. Finally, several  
100 authors couple data by clustering (e.g. Paasche and Tronicke, 2007; Lelièvre  
101 et al., 2012; Sun and Li, 2013) that can be considered more appropriate than  
102 simplified petrophysical assumptions for some geological conditions.

103 The objective of this paper is the introduction and test of a new joint in-  
104 version strategy, in which we try to mitigate the four problems raised above.  
105 Our scheme *JINV2D* is a cell-based non-linear 2-D joint inversion that com-  
106 bines magnetotelluric (MT), seismic P-wave tomography and gravity data  
107 by using petrophysical information and has been mainly developed to in-  
108 vestigate sub-basalt structures that are often not well-resolved by reflection  
109 seismic data. To avoid relative scaling (1st problem) we use a cooperative  
110 joint inversion in which the inversion steps are performed separately for each  
111 method and the otherwise independent inversions are linked by employing  
112 constraints that account for parameter relationships. Core element of our  
113 proposed joint inversion is an automated adaptive coupling scheme, which

114 allows for flexible inclusion of these constraints. This adaptive scheme en-  
115 sures a robust convergence (2nd problem) for all methods and allows the  
116 obtained physical parameter models to deviate from the initial assumed pa-  
117 rameter relationships, which makes this assumption less rigid (4th problem).  
118 Different resolutions of the various methods (3rd problem) are handled by  
119 making the behavior of the coupling constrains dependent on the relative res-  
120 olution power of the methods. Finally, we include a method that allows the  
121 exchange of structural information between the parameter models in addition  
122 to petrophysical information.

123 Within the methodology section we first outline our joint inversion strat-  
124 egy. We then focus on a more detailed description of its implementation.  
125 The adaptive joint inversion scheme is tested on a synthetic model that is  
126 associated with settings that are typical for sub-basalt problems. Finally,  
127 we present joint inversion results from a real data example for sub basalt  
128 imaging from the Faroe-Shetland Basin, where wide angle streamer seismic,  
129 marine MT and marine gravity data are combined.

## 130 **2. METHODOLOGY - OUTLINE OF JOINT INVERSION STRAT-** 131 **EGY**

### 132 *2.0.1. Parametrization*

133 The 2-D grids used for the forward modeling routines are composed of  
134 rectangles to which constant velocity, density and resistivities are assigned.  
135 Cell sizes are adapted individually for each method to account for numerical  
136 accuracy issues and computational efficiency. For the inversion we use a  
137 coarser grid created by combining several forward modelling cells, since the



138 presented inversions (independent on the methods) do not resolve the model  
139 at the numerical precision required for the forward problem. We choose  
140 the same inversion grid for all three methods such that different physical  
141 parameters can be easily linked to each other in the joint inversion and the  
142 method with highest resolution defines the cell sizes to avoid data mismatches  
143 associated with improper discretization.

#### 144 *2.0.2. Forward modeling*

145 Because standard forward modelling techniques are implemented for all  
146 methods we only briefly summarize the routines and refer to the literature for  
147 further information. For seismic tomography first-arrival times are computed  
148 by an eikonal solver (Podvin and Lecomte, 1991) and afterwards the associ-  
149 ated ray-paths are constructed by a steepest descent method (Aldridge and  
150 Oldenburg, 1993). For gravity modelling the z-component of the attractions  
151 from all cells are calculated for each gravity station and the resulting grav-  
152 ity responses are then obtained by summing the contributions from all cells  
153 (Bear et al., 1995). Border effects for the gravity due to the finite extent of  
154 the 2-D model are avoided by adding semi-infinite horizontal rods at the left  
155 and right boundary. For MT we use a 2-D frequency-domain finite-element  
156 code to calculate both the transverse electric (TE) and transverse magnetic  
157 (TM) mode impedances for a number of frequencies (Wannamaker et al.,  
158 1987).

#### 159 *2.0.3. Inversion procedure*

160 A Hessian-free Gauss-Newton minimization method (Nocedal and Wright,  
161 2006), which has a rapid quadratic convergence as long as the local behavior

162 is not strongly non-linear, is used to iteratively solve the linearized inver-  
 163 sion problems. To solve the associated linear system, the LSQR solver from  
 164 Paige and Saunders (1982) is employed. We use first-arrival times of all  
 165 shot-receiver combinations as seismic data ( $\mathbf{d}^{seis.}$ ), the z-component of the  
 166 gravity field at all measuring locations as gravity data ( $\mathbf{d}^{grav.}$ ) and real and  
 167 imaginary part of the impedances for a number of frequencies and at all MT  
 168 stations as MT data ( $\mathbf{d}^{MT}$ ). Model parameters are seismic velocities  $\mathbf{m}^{vel.}$ ,  
 169 densities  $\mathbf{m}^{dens.}$  and logarithmic values of resistivities  $\mathbf{m}^{res.}$  of the inversion  
 170 cells. Smoothing constraints based on Laplacian differences (Ammon and  
 171 Vidale, 1993) are employed as regularization to stabilize the inversion. The  
 172 inversion step lengths are adjusted at every iteration through a line search  
 173 procedure (Moré and Thunent, 1994).

174 Unlike most other joint inversion schemes, the inversion processes of the  
 175 individual methods are performed separately from each other. The required  
 176 coupling between the individual inversions is provided by an additional con-  
 177 straint in the objective function for each inversion accounting for relation-  
 178 ships between the three model parameters  $\mathbf{m}^{res.}$ ,  $\mathbf{m}^{vel.}$  and  $\mathbf{m}^{dens.}$ . We choose  
 179 this approach since it avoids the necessity to find an adequate scaling be-  
 180 tween terms related to different methods in a combined objective function  
 181 (i.e. Moorkamp et al., 2011). However, synchronization between the individ-  
 182 ual processes is required to treat all methods equally. This is achieved by  
 183 performing a single inversion step for all three methods and updating the  
 184 associated coupling constraints before the next iteration is started.

185 For our joint inversion method the objective functions for the MT, seismic

186 and gravity inversion  $\Phi^{MT}$ ,  $\Phi^{seis.}$  and  $\Phi^{grav.}$  are:

$$\begin{aligned}
\Phi^{MT} &= \Phi_{(d)}^{MT}(\mathbf{m}^{res.}) + (\lambda^{MT})^2 \Phi_{(m)}^{MT}(\mathbf{m}^{res.}) + (\mu^{MT})^2 \Phi_{(c)}^{MT}(\mathbf{m}^{res.}, \tilde{\mathbf{m}}^{res.}) \longrightarrow min \\
\Phi^{seis.} &= \Phi_{(d)}^{seis.}(\mathbf{m}^{vel.}) + (\lambda^{seis.})^2 \Phi_{(m)}^{seis.}(\mathbf{m}^{vel.}) + (\mu^{seis.})^2 \Phi_{(c)}^{seis.}(\mathbf{m}^{vel.}, \tilde{\mathbf{m}}^{vel.}) \longrightarrow min \\
\Phi^{grav.} &= \Phi_{(d)}^{grav.}(\mathbf{m}^{dens.}) + (\lambda^{grav.})^2 \Phi_{(m)}^{grav.}(\mathbf{m}^{dens.}) + (\mu^{grav.})^2 \Phi_{(c)}^{grav.}(\mathbf{m}^{dens.}, \tilde{\mathbf{m}}^{dens.}) \longrightarrow min
\end{aligned}$$

187 where  $\Phi_{(d)} = [\mathbf{g}(\mathbf{m}) - \mathbf{d}_{obs.}]^T \mathbf{D}^T \mathbf{D} [\mathbf{g}(\mathbf{m}) - \mathbf{d}_{obs.}]$  are the data terms,  $\Phi_{(m)} =$   
188  $\mathbf{m}^T \mathbf{C}^T \mathbf{C} \mathbf{m}$  are the regularization terms,  $\Phi_{(c)}$  are the terms that account  
189 for the parameter relationships,  $\mathbf{d}_{obs.}$  is the vector containing the observed  
190 data,  $\mathbf{g}(\mathbf{m})$  is the vector containing the calculated data obtained by forward  
191 modeling,  $\mathbf{D}^T \mathbf{D} = \mathbf{C}_{(d)}^{-1}$  is the inverse of the data covariance matrix and  
192  $\mathbf{C}$  is the roughness matrix (containing discrete first-order derivatives). The  
193 impact of the individual terms is governed by the regularization and coupling  
194 parameters  $\lambda^{MT}$ ,  $\lambda^{seis.}$ ,  $\lambda^{grav.}$  and  $\mu^{MT}$ ,  $\mu^{seis.}$ ,  $\mu^{grav.}$ , respectively.

195 While the data terms  $\Phi_{(d)}$  and regularization terms  $\Phi_{(m)}$  are commonly  
196 used in all types of inversions, the coupling terms  $\Phi_{(c)}$  are **particular** to joint  
197 inversion.  $\Phi_{(c)}$  express the coupling between the individual inversions as  
198 minimization problems ( $\Phi_{(c)} \longrightarrow min$ ) and describe, in our case, how far  
199 the model parameters  $\mathbf{m}^{res.}$ ,  $\mathbf{m}^{vel.}$  and  $\mathbf{m}^{dens.}$  deviate from the proposed rock  
200 parameter relationships. To determine the constraints of the  $\Phi_{(c)}$  for all  $N$   
201 inversion cells, projections  $\tilde{\mathbf{m}}$  onto the pre-defined relationship curve are cal-  
202 culated from the physical parameters  $\mathbf{m}$ . The distances between the model  
203 parameters  $\mathbf{m}$  and their projections  $\tilde{\mathbf{m}}$  are then used to define the minimiza-

204 tion problems for  $\Phi_{(c)}$  as:

$$\begin{aligned} \Phi_{(c)}^{MT}(\mathbf{m}^{res.}, \tilde{\mathbf{m}}^{res.}(\mathbf{m}^{res.}, \mathbf{m}^{vel.}, \mathbf{m}^{dens.})) &= \sum_{j=1}^N (m_j^{res.} - \tilde{m}_j^{res.}(m^{res.}, m^{vel.}, m^{dens.}))^2 \\ \Phi_{(c)}^{seis.}(\mathbf{m}^{vel.}, \tilde{\mathbf{m}}^{vel.}(\mathbf{m}^{res.}, \mathbf{m}^{vel.}, \mathbf{m}^{dens.})) &= \sum_{j=1}^N (m_j^{vel.} - \tilde{m}_j^{vel.}(m^{res.}, m^{vel.}, m^{dens.}))^2 \\ \Phi_{(c)}^{grav.}(\mathbf{m}^{dens.}, \tilde{\mathbf{m}}^{dens.}(\mathbf{m}^{res.}, \mathbf{m}^{vel.}, \mathbf{m}^{dens.})) &= \sum_{j=1}^N (m_j^{dens.} - \tilde{m}_j^{dens.}(m^{res.}, m^{vel.}, m^{dens.}))^2 \end{aligned}$$

205 (Note that the all three  $\Phi_{(c)}$  terms are dependent on all three physical pa-  
206 rameters.)

207 Practical meaning of this implementation is that associated constraints  
208 pull the model parameters  $\mathbf{m}^{res.}$ ,  $\mathbf{m}^{vel.}$  and  $\mathbf{m}^{dens.}$  towards the relationship  
209 curves such that the relative behaviour of the different physical models is  
210 approximately described by the parameter relationships.

211 The projection method proposed here (see Appendix A for a detailed  
212 description) has the advantage that the impact of all physical parameters  
213 is equally balanced independent of their parameter ranges. However, it is  
214 only applicable for parameter relationships that have a strictly monotonic  
215 behaviour.

#### 216 *2.0.4. Adjust the projection by using model resolution estimates*

217 Another advantage of the way the projection is implemented is the pos-  
218 sibility to take into account the resolving power of different methods at each  
219 individual cell. In the Appendix B we describe how the projection presented  
220 in Appendix A is modified such that it has the following behaviour: if method  
221 1 (e.g. seismic) has a high resolution and the other methods (e.g. MT and  
222 gravity) have low resolutions in an inversion cell, the resulting parameters

223 from the projection are very similar to the one obtained from the method  
 224 1 e.g. velocity of the projection is very similar to the velocity of the seis-  
 225 mic model and resistivity (density) of the projection are very similar to the  
 226 resistivity (density) calculated from the seismic velocity model by means of  
 227 the parameter relationships (see also black dot in Fig. A.18b in Appendix  
 228 A). If the resolution powers of the different methods are in a similar range,  
 229 the parameters from the projections are averages which are similarly affected  
 230 by all model parameters. Such implementation improves the performance of  
 231 the joint inversion and reduces the number of required iterations to reach  
 232 an adequate data misfit, because the projection direction is guided spatially  
 233 flexible by the relative impact of the different data sets.

234 A good measure for evaluating the resolution of a method is the diago-  
 235 nal of the model resolution matrix  $\mathbf{R} = ((\mathbf{G}^T \mathbf{G} + \lambda^2 \mathbf{C}^T \mathbf{C})^{-1} \mathbf{G}^T) \mathbf{G}$  (where  
 236  $\mathbf{G} = \mathbf{D} \mathbf{S}$  and  $\mathbf{S}$  is the sensitivity matrix).  $\mathbf{R}$  is normalized to 1.0 and 0.0,  
 237 where 1.0 indicates perfectly and 0.0 not resolved at all parameters, respec-  
 238 tively. Retrieving the diagonal by calculating the complete resolution ma-  
 239 trix, however, is difficult for large inverse problems since it requires computer  
 240 memory of the size  $N \times N$ . We therefore use instead an efficient stochas-  
 241 tic estimation of the resolution matrix diagonal suggested by MacCarthy  
 242 et al. (2011). They arrange the equation for the model resolution matrix  
 243 such that its diagonal can be solved with the same linear system as used for  
 244 the corresponding linearized inversion problem (see equations 7 to 9 in their  
 245 publication). (As in their equation 9 we consider the regularization terms  
 246 in the calculation of the resolution matrix diagonal; however, we ignore the  
 247 coupling terms.) Their approach is based on the work from Bekas et al.

248 (2007), who developed a statistical procedure to determine the diagonal of  
249 a large  $P \times P$  matrix by iteratively applying a sequence of  $P$ -length ran-  
250 dom vectors to this matrix. Although the quality of the diagonal estimates  
251 depends onto the number of iterations, we restrict them to maximum 5000  
252 in our runs to keep computation times low. If the diagonal elements are  
253 assigned to the associated inversion cells, the obtained models showing the  
254 resolution estimates appears slightly noisy. To remove this noise and smooth  
255 the resolutions estimates in the spatial directions, the median of resolution  
256 parameters is determined from all neighbouring cells for each cell and applied  
257 as the final resolution measures in the parameter projection.

#### 258 *2.0.5. Adaptive determination of the coupling parameters*

259 In our experience it is necessary need to keep the coupling parameters  
260  $\mu$  flexible during the inversion process. This can be explained as follows.  
261 Each method has its natural convergence path through the model space to  
262 decrease its data misfit. These paths may differ substantially for the different  
263 methods (e.g. MT and seismic tomography are strongly non-linear methods,  
264 whereas gravity is a linear method). Since the projection on the parameter  
265 relationship curve depends on the model parameters of all three methods, **it is**  
266 **possible that, during the inversion process, the natural** convergence direction  
267 for some of the methods points in a completely different direction in the  
268 model space to that the associated coupling constraint points. This can even  
269 occur when the parameter relationships perfectly describe the rock property  
270 behaviour. If the weight of the coupling parameter  $\mu$  is chosen too high,  
271 the associated constraints force the parameter models in wrong directions,  
272 the convergence of the inversion is slowed down and the individual inversion

273 may then get trapped in local minima where the data misfit is not properly  
 274 minimized. In contrast, coupling strengths which are too weak may lead  
 275 to parameter models which are barely linked and, hence, the potential of  
 276 increasing the resolution through joint inversion is then not utilized.

277 To avoid such scenarios we implement a scheme to vary the coupling  
 278 parameters  $\mu^{MT}$ ,  $\mu^{seis.}$  and  $\mu^{grav.}$  for the individual methods adaptively and  
 279 independently from each other during the inversion process. The adaption  
 280 of the coupling parameters is implemented in exactly the same way for all  
 281 three methods and we thus explain the procedure here for one method only.

282 The adaptation criterion is based on the idea that the coupling constraint  
 283 should affect the convergence behaviour of the objective function at each  
 284 iteration,  $k$ , by the same amount. It states that the incremental change of  
 285 the sum of the data and regularization terms of the objective function

$$\Delta\Phi_{(d+m)}^{Constr.,k} := (\Phi_{(d)}^{Constr.,k} + \lambda^2\Phi_{(m)}^{Constr.,k}) - (\Phi_{(d)}^{Constr.,k-1} + \lambda^2\Phi_{(m)}^{Constr.,k-1}) \quad (1)$$

286 for our constrained inversion should correspond to a specified portion  $D$  (with  
 287  $1.0 > D > 0.0$ ) of the same terms

$$\Delta\Phi_{(d+m)}^{Ref.,k} := (\Phi_{(d)}^{Ref.,k} + \lambda^2\Phi_{(m)}^{Ref.,k}) - (\Phi_{(d)}^{Constr.,k-1} + \lambda^2\Phi_{(m)}^{Constr.,k-1}) \quad (2)$$

288 for a reference inversion without constraint ( $\mu_k = 0$ ):

$$\Delta\Phi_{(d+m)}^{Constr.,k} = D\Delta\Phi_{(d+m)}^{Ref.,k} \quad (3)$$

289 The meaning of the criterion is illustrated in Figure 1.

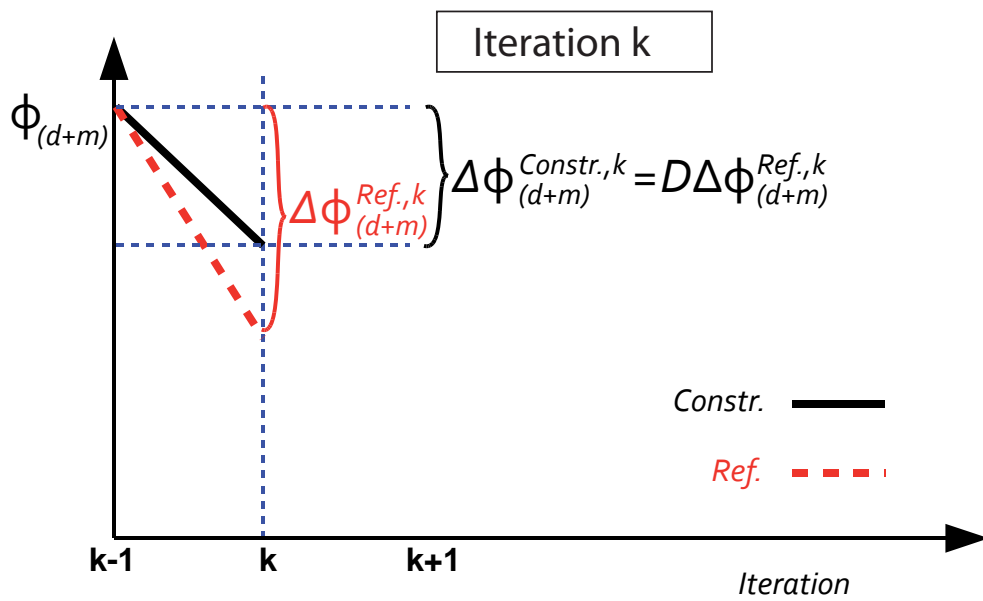


Figure 1: Sketch illustrating the adaptation criterion for the coupling parameters at iteration. The parameter  $\mu$  is chosen such that the change of data term plus regularization term of the objective function  $\Delta\Phi_{(d+m)}^{Constr.,k}$  of the constrained inversion at iteration  $k$  (black line) is a predetermined factor  $D$  smaller than for the change of these terms  $\Delta\Phi_{(d+m)}^{Ref.,k}$  for the unconstrained inversion (red line).



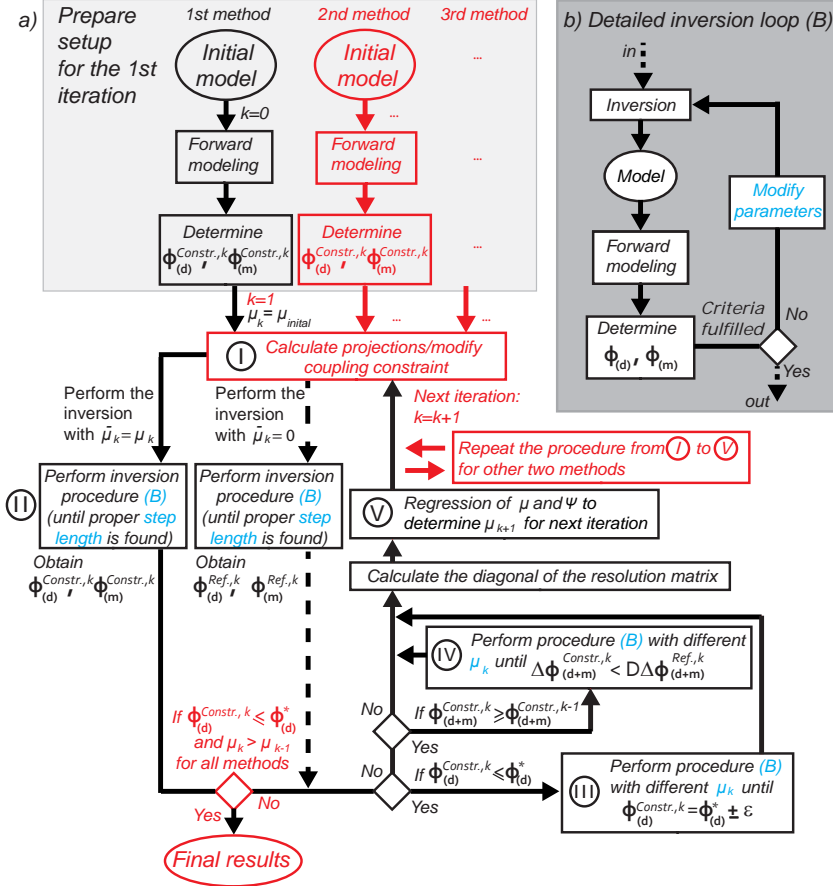


Figure 2: a) Flowchart illustrating the adaptive inversion scheme. The scheme shows the procedure for only one of the methods. For the other methods the procedure is equivalent. Steps where information from the other methods are involved are highlighted in red colors. Roman numerals mark the different steps that are explained in the body of the text. The grey box b) shows an inversion loop, which is performed at different stages of the procedure (see blue letters (B) in a)) and in which the fulfillment of different criteria are tested: At stage II the step length is varied until the Wolfe conditions (Nocedal and Wright, 2006) are satisfied and at stages III and IV  $\mu_k$  is varied until criteria are reached that consider the behavior of the objective functions.

290 Although this criterion specifies how the terms  $\Delta\Phi_{(d+m)}^{Constr.}$  of our con-  
 291 strained inversion should change at each iteration step, it does not explicitly  
 292 depend on  $\mu$ . This means that an additional assumption linking the vari-  
 293 ations of  $\Delta\Phi_{(d+m)}$  with the ones of the  $\mu$  values is required to be able to  
 294 develop an adaptive scheme. Here, we assume that  $\mu$  is approximately linear  
 295 with the normalized incremental change of the objective function  $\Psi_l$  for a  
 296 number of  $L$  successive iterations:

$$\mu_l \approx p_k^{(0)} + p_k^{(1)} \underbrace{\frac{\Delta\Phi_{(d+m)}^{Ref.,l} - \Delta\Phi_{(d+m)}^{Constr.,l}}{\Delta\Phi_{(d+m)}^{Ref.,l}}}_{=:\Psi_l} \quad \text{with } l = k - (L - 1), \dots, k \quad (4)$$

297 To update  $\mu$  at every iteration the criterion and the assumption (eq. 4) are  
 298 combined in the scheme shown in Figure 2.

299 For iteration  $k$ :

- 300 1. the coupling constraint associated with the parameter relationship is  
 301 determined (see ① in Fig. 2)
- 302 2. two model updates (inversion steps) - one with and one without the  
 303 coupling constraint - are performed (see ② and panel (B) in Fig. 2).
- 304 3. forward calculations are conducted for both updated models and the  
 305 associated terms of the objective functions  $\Phi_{(d+m)}^{Constr.,k}$  and  $\Phi_{(d+m)}^{Ref.,k}$  are  
 306 determined. Steps 2 and 3 are repeated with different inversion step  
 307 lengths as long as the step length criteria (Moré and Thuente, 1994)  
 308 are not satisfied (see ③ and box (B) in Fig. 2).
- 309 4. the diagonal of the resolution matrix is calculated to adjust the projec-  
 310 tion.

311 5. a linear regression of normalized incremental change of the objective  
 312 functions  $\Psi_{\tilde{l}}$  and coupling parameters  $\mu_{\tilde{l}}$  from a number of previous  
 313 iterations  $\tilde{l} = k - (\tilde{L} - 1), \dots, k$  is carried out (see  $\odot$  in Fig. 2). The  
 314 axis intercept  $p_k^{(0)}$  and slope  $p_k^{(1)}$  from the linear regression are then  
 315 used to calculate the coupling parameter  $\mu_{k+1}$  for the next iteration by  
 316 means of the formula

$$\mu_{k+1} = (1 - D)p_k^{(1)} + p_k^{(0)} \quad , \quad (5)$$

317 which is obtained by a combination of eq. 3 and eq. 4.

318 6. Steps 1) to 5) are repeated for the other two methods.

319 Steps 1) to 6) are repeated at each iteration.

320 The convergence speed is controlled by the parameter  $D$  and the number  
 321 of previous iterations  $\tilde{L}$ , from which information is used in the regression. For  
 322 larger values of  $D$  it is assumed that the data misfit for the corresponding  
 323 method decreases generally faster during the inversion process (see eq. 3) and  
 324 that the resulting  $\mu$  are smaller (see eq. 5). This means that the associated  
 325 method is less coupled. For larger values of  $\tilde{L}$  the adaptive algorithm reacts  
 326 more inertly if the effect of the relationship constraint onto the convergence  
 327 behaviour changes. On the other hand, regression becomes less sensitive to  
 328 outliers and, hence, the algorithm can be considered as more robust.

329 Regression results and consequently updates of  $\mu$  only depend on the  
 330 distribution of  $\mu_{\tilde{l}}$  and  $\Phi_{\tilde{l}}$  from a small number of previous iterations (typically  
 331  $< 6$ ), therefore updated  $\mu$ 's are only local and not global estimates of the  
 332 best suited values for the coupling at the corresponding iteration. However,  
 333 we tested our scheme on different synthetic examples and observe that the

334 implemented adjustment of coupling parameters is in most cases sufficient  
 335 to obtain stable convergence behaviour for individual inversions. The same  
 336 tests lead us to conclude that  $D$  should be in the range of 0.4 - 0.9 and  $\tilde{L}$   
 337 should be in the range of 2 - 5 to ensure robust and fast convergence.

338 Nonetheless, under some circumstances the assumption of eq. 4 may not  
 339 be appropriate for a specific method and iteration and the determined update  
 340 of  $\mu$  results in an increase of the remaining objective function  $\Phi_{(d+m)}^{Constr.,k} \geq$   
 341  $\Phi_{(d+m)}^{Constr.,k-1}$ . To guarantee convergence, the value of  $\mu_k$  is then recalculated  
 342 in such cases: The inversion loop is repeated for different  $\mu$ -values (see box  
 343 (B) and (iv) in Fig. 2) and by means of interpolation (bisection method)  
 344 an appropriate coupling parameter is found which satisfies the condition  
 345  $\Delta\Phi_{(d+m)}^{Constr.,k} < D\Delta\Phi_{(d+m)}^{Ref.,k}$ . We emphasize that the procedure to recalculate  $\mu$   
 346 is often significantly more time-consuming than determining  $\mu$  by adaption,  
 347 because more forward calculations are required (typically a factor 2-4). Even  
 348 if  $\mu$  values determined from the adaptive procedure provide model updates  
 349 that only roughly satisfy the criterion, it is more useful to take information  
 350 from previous iterations to avoid slowing down the joint inversion process.

351 When the data term of the objective function gets smaller than the speci-  
 352 fied target misfit  $\Phi_{(d)}^{Constr.} \leq \Phi_{(d)}^*$  (typically associated with an error weighted  
 353 data misfit close to 1.0), in principal a solution is found for the associated  
 354 method. Modification of the associated  $\mu$  by the adaptive algorithm is then  
 355 no longer required and one option would be to keep  $\mu$  unchanged in the fol-  
 356 lowing iterations. However, since we are interested in finding the solution  
 357 with the strongest possible coupling, we want to identify instead the largest  
 358  $\mu$  that is compatible with the data. For this purpose, we choose a similar

359 procedure as proposed by Constable et al. (1987) and de Groot-Hedlin and  
 360 Constable (1990), who searches for the smoothest model that explains the  
 361 data (Occam’s inversion). However, in contrast to their approach we consider  
 362  $\mu^{-1}$  (and not  $\lambda^{-1}$ ) as the Lagrangian multiplier that is adjusted when  $\Phi_{(d)}^*$  is  
 363 reached for the associated method. The inversion loop is therefore repeated  
 364 for a number of different  $\mu$  and an interpolation method is employed (bisection  
 365 method) to find the coupling parameter with the largest value which  
 366 satisfies  $\Phi_{(d)}^* - \epsilon \leq \Phi_{(d)}^{Constr.} \leq \Phi_{(d)}^* + \epsilon$  (with  $\epsilon$  being a small positive quantity)  
 367 for the next iteration (see box (B) and  $\textcircled{\text{III}}$  in Fig. 2).

368 The complete inversion procedure stops, when all methods reach their  
 369 specified target misfits and no increase in the coupling parameters can be  
 370 achieved in the next iteration.

### 371 2.0.6. Adjustment of smoothing parameter

372 We have tested different methods to adjust the smoothing during the  
 373 inversion process (including the adaptive scheme used to modify  $\mu$ ). They  
 374 show that the convergence behavior is less influenced by the regularisation  
 375 than by the coupling parameters. Several of the conventional techniques to  
 376 modify  $\lambda$  demonstrate that they are well suited to reach the target misfits and  
 377 we use a simple technique with a cooling-schedule-type behaviour proposed  
 378 by Lelièvre et al. (2012). An initially large value for  $\lambda$  is chosen that is  
 379 reduced with increasing number of iterations. In this way progressively more  
 380 detailed structures are introduced into the models. The factor of reduction  
 381  $1/\nu_k$  from one iteration to the next:

$$\frac{1}{\nu_k} = \frac{\lambda_{k+1}}{\lambda_k} \quad (6)$$

382 is determined by

$$\begin{aligned}\nu_k &= 1 + \tau \left| \Phi_{(d)}^k / \Phi_{(d)}^* - 1 \right| && \text{if } \Phi_{(d)}^k > \Phi_{(d)}^* \\ \nu_k &= 1 && \text{if } \Phi_{(d)}^k \leq \Phi_{(d)}^*.\end{aligned}$$

383 Typical values used for the parameter  $\tau$  are in the range of 0.02 - 0.2. The  
384 rate of reduction depends on the actual target misfit  $\Phi_{(d)}^*$  and  $\nu_k$  remains  
385 constant if the target misfit is reached. To avoid overly fast reduction of the  
386 regularization,  $\nu$  is limited to values between 1 and 2. If a regularization  
387 parameter becomes smaller than a specific threshold value  $\lambda^*$ , the procedure  
388 stops and the regularization remains unchanged ( $\lambda = \lambda^*$ ) for further itera-  
389 tions to avoid instabilities in the inversions. Values for  $\lambda^*$  used in this study  
390 range from 0.7 to 1.0 depending on the methods.

### 391 *2.0.7. Implementation of structural cross-coupling*

392 The adaptive method can be extended to include structural information  
393 at the same time. We have implemented an approach suggested by Günther  
394 and Rucker (2006), where cross-coupling is achieved through mutually con-  
395 trolling smoothing constraints of a given parameter model by the roughness  
396 distribution from other parameter models. Thus a strong spatial parameter  
397 contrast existing in at least one of the parameter models can be transferred  
398 to the other parameter models.

399 This cross-coupling scheme is implemented as follows. Firstly, at the  $k$ -th  
400 iteration the roughness vectors  $\mathbf{r}$  are calculated for all models using:

$$\begin{aligned}
\mathbf{r}^{res.} &= \mathbf{Cm}^{res.} \\
\mathbf{r}^{vel.} &= \mathbf{Cm}^{vel.} \\
\mathbf{r}^{dens.} &= \mathbf{Cm}^{dens.}
\end{aligned}$$

401 where  $\mathbf{C} \in \mathbb{R}^{B \times N}$  is the roughness matrix (where  $B$  is the number of cell  
402 boundaries and  $N$  the number of inversion cells). Secondly, weights  $w_1, \dots, w_B$   
403 are determined for each method by means of the associated roughness vectors:

$$w_j = \min(h_j, 1.0) \quad \text{with} \quad h_j = \left( \frac{\alpha}{\frac{|r_j|}{\|\mathbf{r}\|} + \alpha} + \alpha \right)^\beta \quad (7)$$

where the constants  $\alpha$  and  $\beta$  have typical values of 0.1 and 1.0.

404 Finally, the weights for the model of one method are used to modify the  
405 regularisation terms for the other models:

$$\begin{aligned}
\Phi_{(m)}^{MT} &= \left\| \sqrt{\mathbf{W}^{vel.} \mathbf{W}^{dens.}} \mathbf{Cm}^{res.} \right\|_2^2 \\
\Phi_{(m)}^{seis.} &= \left\| \sqrt{\mathbf{W}^{res.} \mathbf{W}^{dens.}} \mathbf{Cm}^{vel.} \right\|_2^2 \\
\Phi_{(m)}^{grav.} &= \left\| \sqrt{\mathbf{W}^{res.} \mathbf{W}^{vel.}} \mathbf{Cm}^{dens.} \right\|_2^2
\end{aligned}$$

$$\text{with} \quad \mathbf{W} = \text{diag}(w_1, \dots, w_B) \quad (\text{weighting matrix})$$

406 The procedure of this structural cross-coupling strategy is illustrated for  
407 one iteration and two methods in Figure 3. In our inversion scheme the  
408 structural-cross coupling is performed immediately at the beginning of each  
409 iteration (before the coupling constraints for the petrophysical relationships  
410 are calculated; see ① in flowchart in Fig. 2).

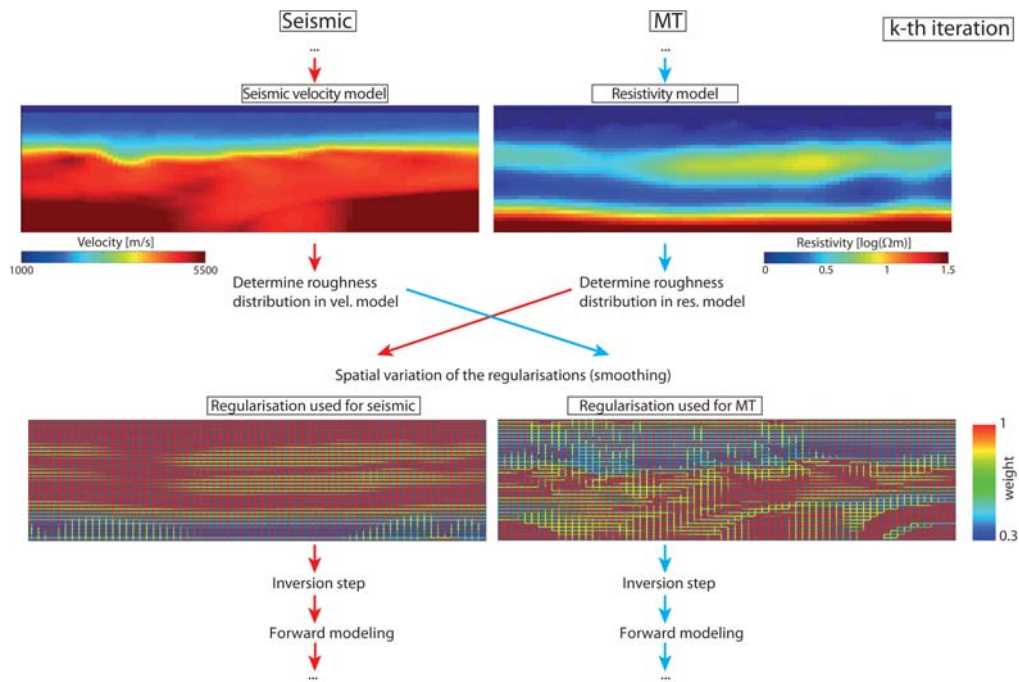


Figure 3: Sketch illustrating the structural cross-coupling strategy proposed by Günther and Rücker (2006). In the upper panel we show a velocity and resistivity model derived at the  $k$ -th iteration for the inversion of seismic tomography and MT data for a synthetic sub-basalt model (see next section for a more detailed discussion). The roughnesses of one model is used to calculate the weights for the smoothing constraints of the other model (see bottom panels); and vice versa.



### 411 3. SYNTHETIC TEST ON A SUB-BASALT MODEL

412 We test our adaptive inversion scheme on a 2-D synthetic basalt model.  
413 The model was proposed by Martini et al. (2005) to simulate realistic seismic  
414 and non-seismic data and to develop strategies for geophysical data integra-  
415 tion for sub-basalt problems. It is known that imaging of sub-basalt sed-  
416 iments with reflection seismic techniques is complicated due to absorption,  
417 scattering and transmission effects and the presence of peg-leg multiples (e.g.  
418 Purnell, 1992). Although many of the difficulties facing conventional seismic  
419 profiles can be overcome by recording long offset data (e.g. Fliedner and  
420 White, 2003), resolution of sub-basalt structures in seismic sections is still  
421 largely limited. Therefore multi-parametric approaches (Hautot et al., 2007;  
422 Panzner et al., 2014; Hoversten et al., 2015) and joint inversion strategies  
423 (Heincke et al., 2006; Colombo et al., 2008; Manglik et al., 2009; Jegen et al.,  
424 2009) have been developed to gain additional information from sub-basalt  
425 structures. Our simplified model contains two mostly horizontal layers that  
426 have high velocity, resistivity and density (Fig. 4, upper panels). The up-  
427 per layer is associated with a sequence of basalt flows and the lower layer is  
428 considered to be basement. Above the basalt and between the basalt and  
429 the basement there are layers with lower physical property values, which rep-  
430 resent sediments over and under the basalt layer, respectively. Everywhere  
431 in the synthetic model the three physical parameters resistivities  $\rho$  (in  $\Omega m$ ),  
432 velocities  $v_p$  (in  $m/s$ ) and densities  $d$  (in  $g/cm^3$ ) are linked by the density-  
433 velocity and resistivity-velocity relationships

$$d = 0.0002 v_p + 1.7 \quad (8a)$$

and

$$\begin{aligned} \log_{10}(\rho) &= 1.20 \log_{10}(v_p) - 3.86 && \text{for } v_p < 3600 \\ \log_{10}(\rho) &= 6.46 \log_{10}(v_p) - 22.57 && \text{for } v_p > 3600 \end{aligned} \quad (8b)$$

434 that are derived from commercial and ODP borehole data collected on  
 435 the north west European margin (Jegen et al., 2009). At the top of the model  
 436 a 400 m thick layer is added representing seawater. Physical properties of the  
 437 water layer remain unchanged during the inversion ( $\rho = 0.3 \text{ } \Omega\text{m}$ ,  $v_p = 1560$   
 438  $\text{m/s}$ ,  $d = 1.0 \text{ g/cm}^3$ ). The model is discretized for inversion into  $85 \times 71$  cells  
 439 with sizes of  $400 \times 100$  m in the horizontal and vertical directions, respectively.

440 The seismic and gravity data sets for the synthetic tests are generated  
 441 using the same forward modeling routines as in the joint inversion. However,  
 442 to reduce the impact of modelling effects that are associated with using the  
 443 same forward codes, discretisations of the model for data generation are  
 444 significantly finer than the ones used in the forward modeling routines during  
 445 inversion. For MT we employ a different modelling program (2-D MT code  
 446 from Tarits, 1984) to calculate the impedance estimates from the synthetic  
 447 model to the one (2-D MT code from Wannamaker et al., 1987) we use in  
 448 the joint inversion.

449 For seismics we consider an OBS data set with 6018 first arrivals from  
 450 177 shot and 34 receiver positions, respectively. Both shot positions at the  
 451 surface and receivers at the seafloor are equally spaced ( $\Delta x_{\text{shots}} = 200$  m  
 452 and  $\Delta x_{\text{receivers}} = 1000$  m). The gravity data set is composed of 60 stations

453 located on the sea surface ( $\Delta x_{\text{grav. station}} = 500$  m). The MT data set consists  
454 of 33 stations that are equally spaced along the seafloor ( $\Delta x_{\text{MT station}} = 1000$   
455 m). Such short station intervals are still uncommon for MT field surveys.  
456 However, the objective of this exercise is to evaluate the general performance  
457 of our joint inversion scheme and at this stage we prefer to use models, where  
458 the individual methods show a dense and uniform coverage. We use as input  
459 for the inversions both TE and TM mode data with 15 frequencies over a  
460 range of  $2.5 \cdot 10^{-5}$  to 1 Hz. Gaussian noise is added to all data sets with  
461 standard deviations  $\sigma_{\text{seis.}} = 10$  ms,  $\sigma_{\text{grav.}} = 0.05$  mgal and  $\sigma_{\text{MT}} = 2\%$  of the  
462 abs. values, respectively.

463 To obtain a qualitative understanding about the resolution power of the  
464 individual methods we plot estimates of the diagonal elements of the reso-  
465 lution matrix (Fig. 4, lower panels) for the synthetic model. Based on this  
466 measure, seismic rays from first arrivals only provide information about the  
467 top of basalt and the overlying sediments. Resolution of gravity data varies  
468 smoothly and decreases with depth, as is typical for potential field methods.  
469 MT is sensitive to the conductive sediments, but not to the highly resistive  
470 basalt layer and basement. At the left and right border high resolution values  
471 in the (gravity and) MT are related to a background layer model required  
472 for both methods (gravity: semi-infinite horizontal sheets; MT: cells at the  
473 border, whose size increasing with the distance from the model boundary).  
474 The resolution estimate shows that all three methods are sensitive to differ-  
475 ent subsets of structural elements of the model and thus contain common but  
476 also complementary information about the entire structure. It is the com-  
477plementary information content in the data sets which allows the derivation

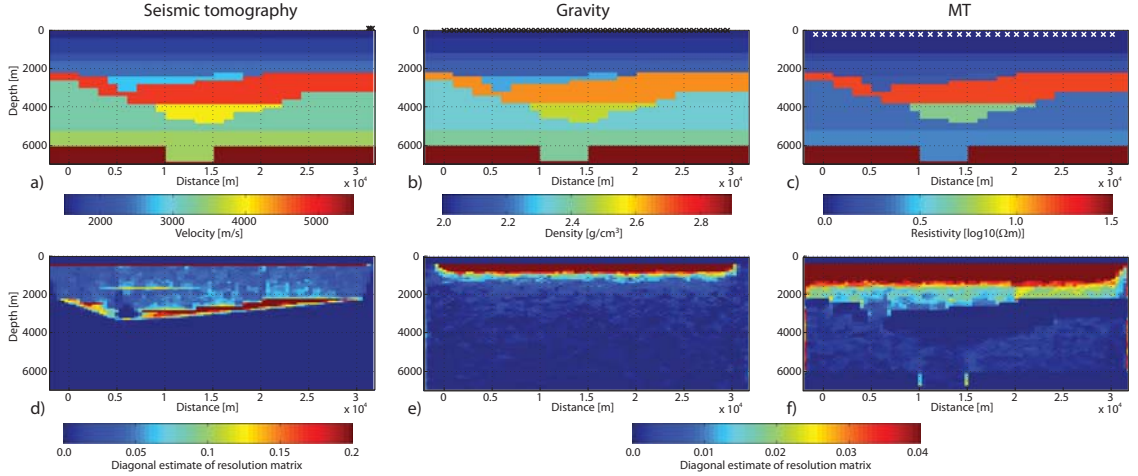


Figure 4: Upper panels: a) Velocities, b) densities and c) resistivity distributions representing the synthetic sub-basalt model. Circles denote locations of OBS stations and crosses highlight positions of shots in a), gravity stations in b) and MT stations in c). Lower panels: Approximations of the diagonal elements of the resolution matrices for each method (see section 2.0.4 for further details about their calculation). High values of resolution are found at the very right and left border of the gravity and MT data (see panels e,f) due to necessity to include a background gravity and MT model.

478 of an improved model through a joint inversion process.

### 479 3.1. Results from the individual inversions

480 Before presenting the results of the joint inversion we show results of in-  
 481 verting each of the datasets separately. For seismic inversion we use a starting  
 482 model that consists of horizontal velocity layers, but for gravity and MT in-  
 483 versions starting models are homogenous half-space models. Cell sizes are  
 484 the same as in the joint inversion. In contrast to the joint inversions, a con-  
 485 ventional Occam's type inversion is performed for the individual inversions;

486 i.e. if the target misfit is reached in the inversion procedure,  $\lambda$  is adjusted to  
487 find the smoothest model that explains the data.

488 Results of these individual inversions (Fig. 5, Row 1) show that none of  
489 the three methods is able to resolve the basalt layer, the underlying sediments  
490 and the basement at the same time, which confirms our prediction based on  
491 the resolution analysis. Refraction seismic tomography only resolves the ve-  
492 locity distribution down to the top of basalt. The gravity inversion does not  
493 resolve any structure. The MT inversion identifies high and low resistive  
494 structures that can be associated with the basement and conductive sedi-  
495 ments, respectively, however the resistive basalt layer is not well resolved  
496 (too low resistivities and inaccurate shape).

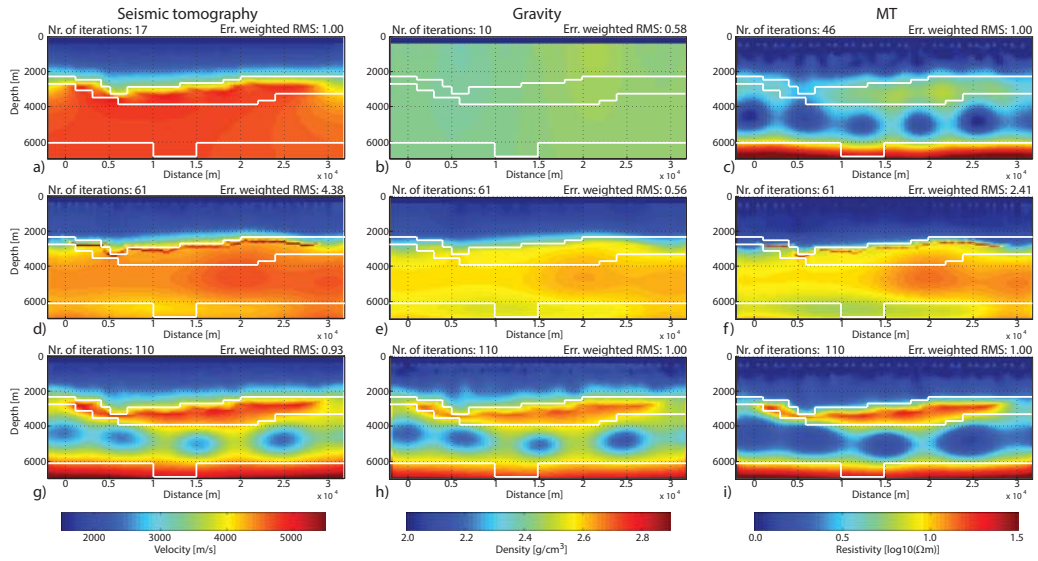


Figure 5: First row: Final results from individual Occam seismic, gravity and MT inversions. Second row: Final results from a petrophysical joint inversion, in which the strengths of coupling is kept constant ( $\mu^{MT} = \mu^{seis.} = \mu^{grav.} = 0.25$ ) during the inversion process. Third row: Final results from a petrophysical joint inversion, in which the coupling constraints are adapted at each inversion step (rate of adaption  $D^{MT} = D^{seis.} = D^{grav.}$  is 0.7 and 3 previous iterations  $\tilde{L}$  are considered in the regression). Unlike in the tests presented in Fig. 6 the projection is not modified by a resolution measure. Locations of the basalt layer and the basement are outlined with white lines.

497 *3.2. Starting models for the joint inversions*

498 To determine the starting models for the joint inversions, first, individual  
499 seismic tomography inversion is performed. We then use the parameter rela-  
500 tionship (eq. 8a) to transfer the initial velocity model to a density model. For  
501 this model an individual gravity inversion is performed. During this gravity  
502 inversion, density values of cells covered by seismic rays are kept fixed. Model  
503 densities from the inversion results are finally transferred back to velocities  
504 and also resistivities (eqs. 8a and 8b). This procedure determines starting  
505 models that are already relatively close the actual subsurface; a strategy  
506 commonly used in joint inversion applications. We demonstrate later in this  
507 section that we obtain similarly good final joint inversion results by using  
508 starting models that are not linked to each other and are further away from  
509 the true model.

510 *3.3. Results from petrophysically linked joint inversions*

511 First, we test our joint inversion scheme with coupling parameters that  
512 remain constant during the inversion process ( $\mu^{seis.} = \mu^{grav.} = \mu^{MT} = 0.25$ ).  
513 All methods are equally weighted for projections onto the parameter rela-  
514 tionships, which means the resolution of each of the methods is not taken  
515 into account. We also do not include structural cross coupling, however, we  
516 gradually reduce the smoothing parameters (from starting values of  $\lambda^{seis.} =$   
517  $\lambda^{grav.} = \lambda^{MT} = 0.25$ ) as described in the section 2.0.6. The final results for  
518 this test are not satisfying (Fig. 5, Row 2); the shape of high velocity, resis-  
519 tivity and density anomalies does not coincide with the shape of the basalt  
520 in our synthetic model and there are no low velocity, resistivity nor density  
521 anomalies can be associated with sub-basalt sediments. Error weighted data

522 misfits  $d_{RMS} = \sqrt{\frac{1}{M} \sum_{i=0}^M \left(\frac{g(\mathbf{m})_i - d_i}{\sigma_i}\right)^2}$  do not reach the target misfit of 1.0 for  
 523 seismic ( $d_{RMS}^{seis.} = 4.38$ ) and MT ( $d_{RMS}^{MT} = 2.41$ ), respectively. It is likely that  
 524 the inversion processes get trapped in local minima relatively close to the  
 525 actual starting models. (In contrast, the error weighted data misfit for the  
 526 gravity  $d_{RMS}^{grav.} = 0.56$  remains clearly smaller than the target misfit of 1.0, al-  
 527 though  $\lambda$  is increased, when the target misfit is reached (Occam’s inversion).  
 528 This indicates that the amount of smoothing has little impact onto the data  
 529 misfit of the gravity.)

530 In the next step the joint inversion is repeated using the same starting  
 531 model and initial coupling values, however, now we adaptively modify our  
 532 coupling parameters.  $D$  is set to relatively high values of  $D^{seis.} = D^{grav.} =$   
 533  $D^{MT} = 0.7$  to control the convergence rate. The number of previous itera-  
 534 tions  $\tilde{L}$  used to predict the  $\mu$ -value for the next iteration is 3 for all methods.  
 535 Otherwise, the starting models and other settings are the same as for the  
 536 previous test.

537 The resulting models (Fig. 5, Row 3) are now significantly closer to the  
 538 synthetic model (Fig. 4, Row 1). Two high-velocity (high-density, high-  
 539 resistivity) anomalies are present in the middle and the bottom of the model.  
 540 Their positions (and the shape of the upper anomaly) fit well with the two  
 541 layers representing the basalt and the basement. The region between the  
 542 two layers has lower values of the physical properties and can be associated  
 543 with the sub-basalt sediments. However, the presence of some artificial ”egg-  
 544 shaped” anomalies in this part of the model indicates the limits in resolution  
 545 of the joint inversion. In addition, the objective functions of all three meth-  
 546 ods decrease at each individual iteration until the associated target misfit



547 is reached (Fig. 7d)) and final error weighted data fit from all three meth-  
 548 ods largely match the target misfit of 1.0 indicating a proper convergence  
 549 behaviour. Only few iterations (2 and 4) are required to reach the target  
 550 misfits for the gravity and seismic data, respectively, however many itera-  
 551 tions (101) are required for MT. To some extent this slow convergence be-  
 552 haviour seems to be inherent to the synthetic model **as already** the individual  
 553 MT inversion requires 45 iterations to reach the target misfit. Furthermore  
 554 the criterion used in the joint inversion (i.e.  $\Phi_{(d+m)}$  of the joint inversion  
 555 with coupling constraint decreases only by a portion of the one of the uncon-  
 556 strained inversion) reduces the convergence speed compared to the individual  
 557 MT inversions and for a value of  $D^{MT} = 0.7$  one would expect that about  
 558  $45/0.7 \approx 64$  iterations to be needed to reach the target misfit. One reason  
 559 why almost double as many iterations are needed could be that the projec-  
 560 tion linking the individual physical models is far from an optimum and this  
 561 slows down the overall inversion convergence.

562 In section 2.0.4 we discuss that the convergence behaviour may improve if  
 563 the projection is controlled by the relative resolution power of the individual  
 564 methods. Therefore we repeat the joint inversion test, but in this case the  
 565 diagonal of the resolution matrix is used to weight the individual methods in  
 566 the projection calculation (see section 2.0.4). Final results (compare Fig. 6,  
 567 Row 1, with Fig. 5, Row 3) are very similar, however, the convergence for the  
 568 MT method is 20% faster (compare Fig. 7d) and Fig. 7e)). In addition, the  
 569 updates of  $\mu^{MT}$  that are determined from the linear regression are now more  
 570 reasonable (i.e.  $\Phi_{(d+m)}^{MT, Constr.}$  decreases) for most iterations and a readjustment  
 571 of  $\mu^{MT}$  by using the loop  $\textcircled{\text{IV}}$  (see Fig. 2) is only required for 2 iterations

572 (Fig. 7b)). In contrast, if the resolutions estimates are not considered in the  
 573 projection (Fig. 7a),  $\mu^{MT}$  has to be readjusted for at approx. 30 iterations.  
 574 Based on these observations (and other synthetic examples not shown here),  
 575 convergence seems faster and more stable, if resolution is incorporated in the  
 576 calculation of the parameter projections.

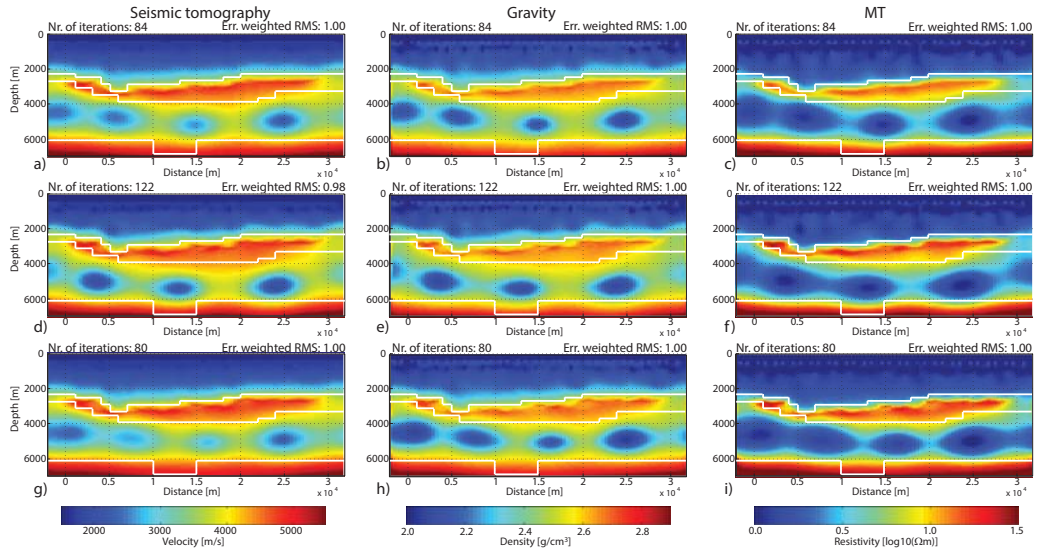


Figure 6: Final results from joint inversions, for which the strengths of coupling vary adaptively during the inversion process. For all tests shown here physical parameter projections are determined by considering relative resolution power of each method (see section 2.0.5). First and second row: Results from two tests, where different rates of adaption  $D^{seis.} = D^{grav.} = D^{MT}$  of 0.7 and 0.4 are employed. Third row: Results from a test with other starting models (layered velocity model and homogenous half-space model for density  $2.4g/cm^3$  and resistivity of  $10\Omega m$ ). Otherwise the same parameters are employed as for the run, whose results are shown in the first row.

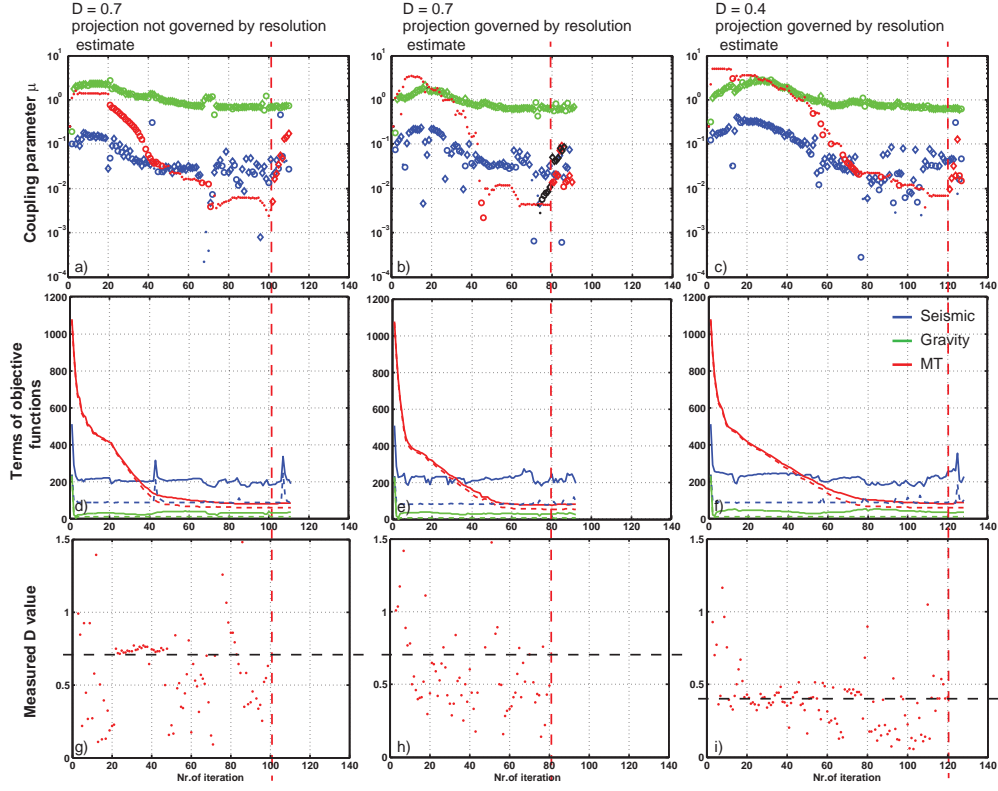


Figure 7: Behavior of the adaptive joint inversions from Figs. 5g)-i), Figs. 6a)-c) and Figs. 6d)-f) are shown in columns 1, 2 and 3, respectively. In all graphs blue refers to seismic, green to gravity and red to MT inversion parameters, shown as a function of iteration number. First row: Coupling parameters  $\mu^{MT}$ ,  $\mu^{seis.}$  and  $\mu^{grav.}$ . The symbols ( $\diamond$ ) and ( $\circ$ ) indicate iterations, where the procedures III and IV (see Fig. 2) are active, respectively. Second row: Values of total objective functions (continuous lines) and their data terms (dashed lines). Third row: Ratio  $\tilde{D}^{MT}$  of the incremental changes of the total objective functions for inversions without and with coupling constraints. This ratio is here only shown for the MT data, because the target misfits for the other methods are reached after very few iterations ( $< 5$ ). Black dashed lines mark the associated pre-defined rate of adaption  $D^{MT}$ . Vertical red dashed lines indicate the iterations for which the target misfits are reached for all three methods.

577 For all adaptive joint inversions tests presented here, the inversion run is  
 578 not terminated immediately after target misfits are reached for all methods,  
 579 but continued for some additional iterations. As described in section 2.0.6,  
 580 this strategy is adopted from Occam’s inversion (see also loop ④ in Fig. 2).  
 581 Because three parameters ( $\mu^{MT}$ ,  $\mu^{seis.}$ ,  $\mu^{grav.}$ ) are adjusted simultaneously, it  
 582 is difficult to find uniquely defined stopping criteria that reliably work for all  
 583 types of models, methods and data sets. We therefore stop the joint inversion  
 584 manually, when one of the coupling parameters shows a significant decrease  
 585 for a few subsequent **iterations**. We generally observe that the model results  
 586 are slightly better (**i.e. in particular the physical properties of the basalt layer**  
 587 **are higher and closer to the ones of the synthetic model**) if the procedure is  
 588 not terminated immediately after all target misfits are reached.

### 589 3.3.1. Impact of the parameters $D$ onto the joint inversion behaviour

590 As discussed in section 2.0.5, the parameters  $D$  have in theory a large  
 591 impact on the convergence speed for the associated methods. To investigate  
 592 this in more detail, the previous joint inversion test is repeated with the  
 593 same settings as before except for a lower value for  $D^{seis.}$ ,  $D^{grav.}$  and  $D^{MT}$   
 594 of 0.4. Obtained final models are very similar to the ones from the previous  
 595 inversion run where  $D = 0.7$  is used (Rows 1 and 2 in Fig. 6). However, as  
 596 expected for decreased  $D$  values we require now significantly more iterations  
 597 (120 compared to 81 iterations with higher  $D$  values) to reach the given target  
 598 misfit (Fig. 7e) and f)). We also observe that the coupling parameter  $\mu^{MT}$   
 599 has generally slightly higher values for a lower  $D^{MT}$  than for a larger  $D^{MT}$   
 600 values (Fig. 7b) and c)). This can be explained by the general behaviour of  
 601 inversions that slower convergence correlates with stronger constraints.

602 *3.3.2. Validation of the linear assumption of  $\mu$  and  $\Psi$*

603 The linear assumption between the coupling parameters  $\mu$  and the nor-  
 604 malized changes in the objective functions  $\Psi$  in eq. 4 is intuitively made.  
 605 Therefore we now test if it is appropriate and evaluate its effect on the ef-  
 606 ficiency of the joint inversion. The assumption can be considered as appro-  
 607 priate as long as the modified  $\mu$  from the regression provide a convergent  
 608 behaviour (i.e. a decrease of  $\Phi_{(d+m)}^{Constr.}$ ). For our joint inversion runs, the MT  
 609 part shows a convergent behaviour for most iterations (see small red dots  
 610 in the Figs. 7a)-c)). Particularly the run, where we use large  $D$ -values of  
 611 0.7 and employ a resolution measure in the projection calculation, exhibits  
 612 convergent behaviour for all but two iterations (see Fig. 7b and section 3.3).

613 To obtain a more quantitative measure to evaluate the validity of our  
 614 assumption, we calculate for each method and for each iteration  $k$ :

$$\tilde{D} = \frac{\Delta\Phi_{(d+m)}^{Constr.,k}}{\Delta\Phi_{(d+m)}^{Ref.,k}}. \quad (9)$$

615 If the assumption is perfectly valid,  $\tilde{D}$  would equal  $D$ . For the test run  
 616 with  $D^{MT} = 0.4$  we obtain a similar median of the  $\tilde{D}^{MT}$  values of 0.378 and  
 617 relatively low scatter of the  $\tilde{D}^{MT}$  values with a  $\sigma^2 = 0.042$  (Fig. 7i)), if we  
 618 only consider  $D$ -values from iterations in which  $\mu$  values are not modified by  
 619 loop (iv). It indicates that the linear regressions provide updates of coupling  
 620 parameters which seem to satisfy the assumption. For a larger  $D^{MT}$ -value of  
 621 0.7, a larger discrepancy of the median value (0.508) and a larger variance  
 622 of  $\sigma^2 = 0.42$  suggest that the assumption is less appropriate (Fig. 7h). We  
 623 have made several further tests with other  $D$ -values that confirm that a lower  
 624  $D$ -value results in a better controlled convergence behaviour.

625 At first glance, the better controlled convergence for low  $D$ -values appears  
626 to contradict the previous observation that convergence failed for fewer itera-  
627 tions when higher  $D$ -values are used. However, one has to consider that lower  
628  $D$ -values (eq. 3) result in a slower convergence such that already a small scat-  
629 ter of the  $\tilde{D}$ -values can result in an increase of  $\Phi_{(d+m)}^{Constr.}$  at any iteration. In  
630 summary, it is not easy to draw any general conclusions, for which  $D$ -values  
631 the assumption provides a convergent behaviour for most iterations. This  
632 is probably highly dependent on the methods involved and other settings of  
633 the actual inversion.

### 634 3.3.3. Dependence of the starting model

635 We repeat the joint inversion test with  $D^{seis.} = D^{grav.} = D^{MT} = 0.7$  with  
636 different starting models, which are not linked by the parameter relationships  
637 and are further away from the synthetic model. Homogenous half-space mod-  
638 els with  $2.4g/cm^3$  and  $10\Omega m$  are chosen for the gravity and MT inversions,  
639 respectively, and a layered velocity model is taken for the seismic inversion.  
640 Final results are similar to the ones from the joint inversion having the same  
641 parameter settings, but starting models that are linked by parameter rela-  
642 tionships (see section 3.3) (compare the Rows 1 and 3 in Fig. 6). Convergence  
643 speed of gravity and seismic inversion is similar, but MT inversion reaches  
644 the target misfit even faster after 67 iterations compared to 81 iterations.

645 The choice of the starting model seems not critical for conditions, where  
646 the total resolution of the joint inversion is rather high and all models explain-  
647 ing the data are similar. We attribute this to the observation that adaption  
648 of the coupling strengths reduces the risk that the inversions get stuck in a  
649 local minima.

650 *3.4. Results from joint inversions using both petrophysical and structural in-*  
651 *formation*

652 To further improve the results from the petrophysical inversion we now  
653 add structural information. First, we test a purely structural joint inversion  
654 using the mutual cross-coupling strategy described in the methodological  
655 section 2.0.7. The weights applied to the discrete derivative matrix  $\mathbf{C}$  are  
656 calculated using values of 0.1 and 1.0 for the parameters  $\alpha$  and  $\beta$  in eq. 7,  
657 respectively. As starting models the same linked parameter models are used  
658 as described before.

659 This joint inversion run gets stuck in some local minima and misfits for  
660 seismic (minimum  $d_{RMS}^{seis.} = 4.72$ ) and MT (minimum  $d_{RMS}^{MT} = 2.64$ ) and  
661 do not reach the target misfits. We conclude that starting models close to  
662 the synthetic models are required to such that this approach is successful.  
663 And although our starting models are derived from the final results of the  
664 individual inversions they are still too inaccurate to provide conditions for  
665 the structural joint inversion to converge. We note that other studies using  
666 this coupling strategy successfully combine geophysical methods with higher  
667 resolutions (e.g. seismic tomographic and electrical resistance tomography,  
668 Günther and Rücker, 2006), where the starting models obtained from indi-  
669 vidual inversions are close enough to the true subsurface conditions to ensure  
670 convergence of the joint inversion.

671 Based on this observation, we choose as starting models for the combined  
672 structural and petrophysical joint inversion the models from the 72th itera-  
673 tion of the adaptive joint inversion with  $D^{seis.} = D^{grav.} = D^{MT} = 0.7$  and  
674 a resolution measure in the projection calculation. **In all three parameter**

675 models locations of main anomalies are overlapping such that it can be as-  
676 sumed that these starting models are close enough to the synthetic model for  
677 the inversion to converge. Target misfits for all methods are reached after  
678 few iterations ( $< 6$  for all methods). The coupling parameters are generally  
679 slightly higher than for the corresponding purely petrophysical joint inversion  
680 (see black symbols in Fig. 7b), probably due to the fact that overall smooth-  
681 ing is reduced by cross-coupling such that more coupling is required to obtain  
682 the same data misfits as for the inversion without structural linkage.

683 Final results (Fig. 8) show that this combined structural and petrophys-  
684 ical joint inversion resolves the main structures as well as the purely petro-  
685 physically coupled joint inversion. However, the boundary between the up-  
686 per sediments and the basalt is now sharpened in all three parameter models  
687 (compare with results in Fig. 6) and its location coincides well with upper  
688 sediments-basalt interface in the synthetic model. This demonstrates that  
689 a combination of both structural and petrophysical linkage further improves  
690 joint inversion results.

#### 691 4. Real data example

692 We apply our joint inversion scheme to data recorded about 150 km south-  
693 east of the Faroe Islands (Fig. 9). This area is characterized by thick se-  
694 quences of basalt flows that are associated with magmatic activity during  
695 the continental break-up of the North Atlantic in the Tertiary (e.g. White  
696 et al., 2003; Gallagher and Dromgoole, 2007). The basalt flows overlie sed-  
697 iments accumulated in basins during earlier episodes of stretching of the  
698 continental lithosphere from the late Carboniferous to the early Paleocene.



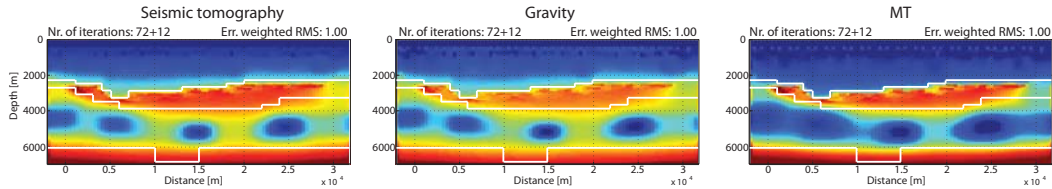


Figure 8: Final results for a joint inversion, which combines the adaptive coupling strategy considering petrophysical information with mutual cross-coupling strategy considering structural information. Starting models for this run are the intermediate results (72 iteration) of the petrophysical inversion, whose results are shown in Figure 6. For this inversion  $D$  values are set to 0.7 and resolution estimated are incorporated in the calculation of physical parameter projections.

699 Traps in these Mesozoic sub-basalt sediments are considered as potential  
700 hydrocarbon-bearing structures. Underneath the sediments a pre-rifted base-  
701 ment is present which probably consists of gneissic rocks and formed during  
702 the Caledonian Orogeny.

703 In this area comprehensive geophysical data sets are available for a wide-  
704 range of methods. *Statoil*, who manages License L006 (red outline in Fig. 9)  
705 in this region, provided us with geophysical data presented here. The data  
706 include a pattern of wide-angle seismic lines, a marine 3-D Full Tensor Grav-  
707 ity (FTG) survey and a number of MT sites distributed on a 3-D grid. While  
708 the data provide 3-D coverage, we limit our investigation to 2-D lines, since  
709 *JINV2D* cannot handle 3-D MT data. We therefore focus on the FLA6  
710 profile, which crosses the northern part of the license area in WNW-ESE  
711 direction (green line in Fig. 9). Hence in the joint inversion presented here  
712 we only use seismic data from FLA6 (49093 seismic first arrival times from  
713 shot gathers that have offset ranges of 3 to 18km) and gravity (425 locations

714 from a 3-D shipborne survey) and MT data (11 stations with periods from  
715 0.0061 to 0.15 s) that are measured in the vicinity of this profile.

716 Data from the individual methods were collected in separate surveys from  
717 1995 to 2002 and the acquisition strategies are not optimized for such data  
718 integration. MT stations used in our 2-D joint inversion are not located  
719 immediately on the seismic profile but lie up to 7 km on either side of it.  
720 MT and gravity data only overlap with seismic data in the western and  
721 eastern part of the profile (Fig. 9), respectively. In addition to the geophysical  
722 data used for the inversion, we received data from a 3-D reflection seismic  
723 survey, which has a large overlap with the FLA6 profile in the northern  
724 part of the licence, and logging data from the 4200 m deep BRUGDAN well  
725 located in the immediate vicinity of the FLA6 profile (red star in Fig. 9).  
726 The reflection seismic data allow a direct comparison of the joint inversion  
727 results with structures derived independently. We use the logging data (sonic,  
728 resistivity and gamma-gamma log) to derive parameter relationships for our  
729 joint inversion, which are depth independent.

730 The nearly vertical BRUGDAN borehole penetrates the top basalt and  
731 the underlying sediments at 1154m and 3719m below sealevel, respectively  
732 (Schuler et al., 2012). Logging data show a distinct increase in P-wave veloc-  
733 ities and resistivities across the upper sediment-basalt interface (see Fig. 10).  
734 (Although no density data from logging are available above the basalt, it is  
735 likely that densities of the basalt are significantly higher than of the shallow  
736 sediments.) The possible base of the basalt sequence is however character-  
737 ized by a more gradual change in physical parameters. Figures 11a) and b)  
738 show cross-plots and we observe that there are positive correlations between

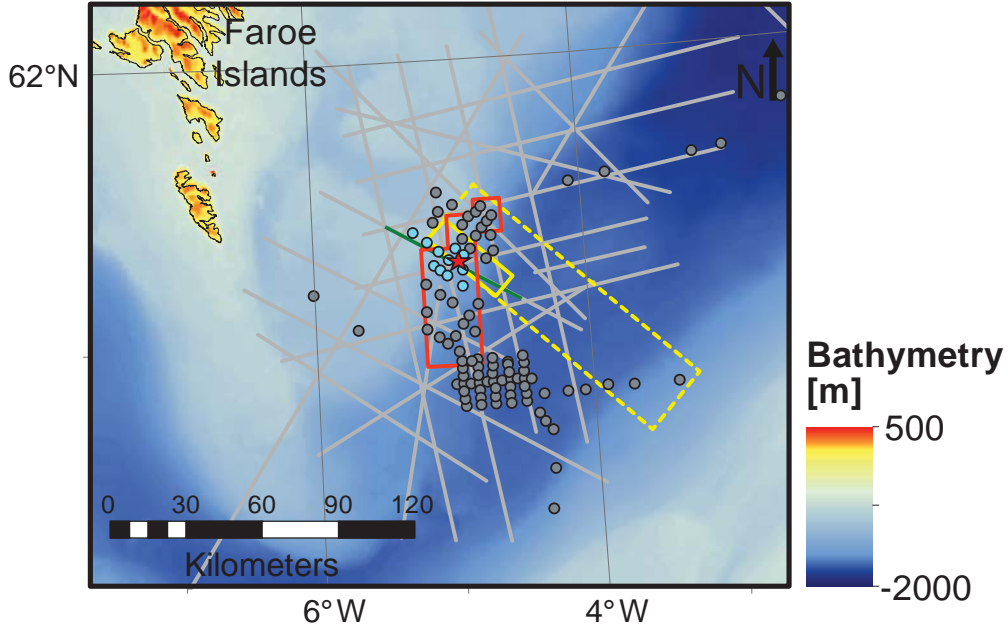


Figure 9: Map of our investigation area in the Faroe-Shetland Basin. A FTG survey (dashed yellow rectangle), several wide angle seismic profiles (grey lines) and MT sites (circles) are present in the region. Data used in our 2-D joint inversion along the seismic profile FLA6 are highlighted (small yellow rectangle, green line and light blue circles correspond to the gravity, seismic and MT data, respectively). Red star indicates the position of the BRUGDAN borehole, red line outline the license area L006.

739 seismic P-wave velocity and resistivity and between P-wave velocity and bulk  
 740 density. Such positive  $v_p$ - $d$  correlations are present for many subsurface con-  
 741 ditions, but positive  $v_p$ - $\rho$  correlations are less common and are reported for  
 742 fewer **geological** conditions e.g. for sub-basalt regions due to the effect of the  
 743 pore space on both  $v_p$  and  $\rho$  (e.g. Jegen et al., 2009).

744 To estimate adequate parameter relationships for the joint inversion,  
 745 curve-fitting in a least-square sense was performed between the physical prop-

746 erties of the borehole logging data (Fig. 11a)-b)). The analytic expressions  
 747 are

$$748 \quad \log_{10} \rho = 7.876 \cdot 10^{-8} \cdot (v_p)^2 - 0.1512$$

$$749 \quad d = 0.0001737 \cdot v_p + 1.868$$

750 for the velocity (in  $m/s$ ) - resistivity (in  $\Omega m$ ) and velocity (in  $m/s$ ) - density  
 751 (in  $g/cm^3$ ) relationships, respectively.

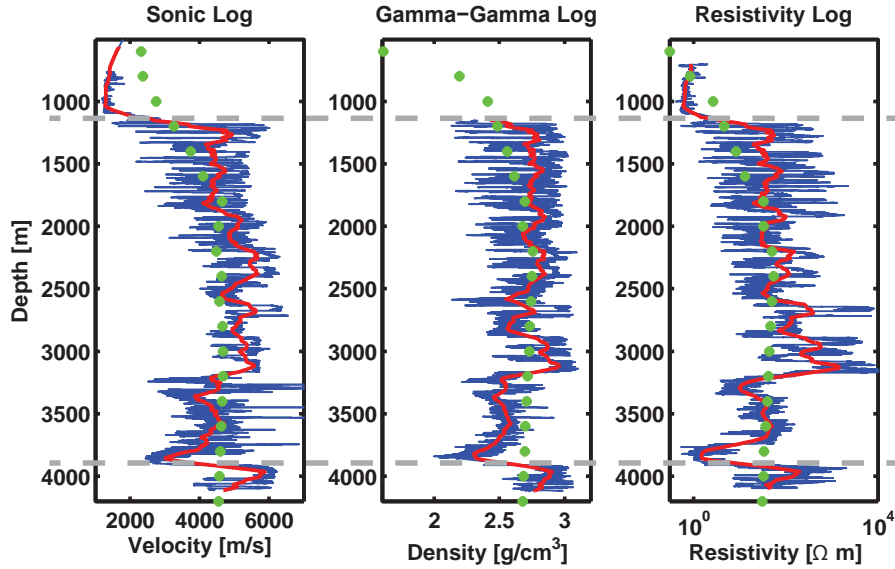


Figure 10: Comparison of the logging data from the BRUGDAN borehole and the joint inversion results along the prole FLA6. Blues lines show measured borehole logs and red lines the same data after applying a moving average (filter length = 100 m). Green dots indicate the physical properties obtained from the joint inversion along the borehole drilling (see Fig. 17). Horizontal grey dashed lines indicate top and base basalt as proposed by Schuler et al. (2012).

752 The logging data generally show a large variation of the physical proper-  
753 ties on a sub-metre scale. Cross plots of the physical parameters (Fig. 11)  
754 show that this results in a larger scatter around the fitted relationships and  
755 reveal that for some geological structures rock property links are systemati-  
756 cally shifted (e.g. depth range 2500-3150 m in Fig. 11a-b) such that the fits  
757 are not good representations for these depths ranges. However, if the logging  
758 data are averaged over depths intervals of 100m, which corresponds to the  
759 cells widths in the inversion, the relationships are adequate estimates for the  
760 scale resolvable by the inversions (Fig. 11c-d)).

#### 761 4.1. Estimation of data errors

762 It is crucial for our adaptive joint inversion scheme to use realistic data er-  
763 ror estimates, as the coupling strength of a method is strongly dependent on  
764 the level of the associated target misfit (at later iterations when the loop ③ in  
765 Fig. 2 becomes relevant). For seismic and gravity we estimated errors directly  
766 from the available data. For a number of seismic shot gathers first-arrivals  
767 were picked independently by three experienced persons. A meaningful offset  
768 dependent error estimates for all seismic data is derived by considering the  
769 time variations of the three picked onsets for the same traces. For the grav-  
770 ity the data spacing of measurement points in the in-line direction is small  
771 ( $\approx 15m$ ) and the ocean is several hundred meters deep such that variations  
772 with short wavelength can be associated with uncorrelated noise. We there-  
773 fore obtain a proper error estimate ( $\sigma^2 = 0.1mgal$ ) through experimental  
774 **variograms at very small distances ("nugget" effect; see e.g. Dubrule, 2003).**  
775 For MT we only received processed data as frequency dependent impedance  
776 estimates together with some error estimates (determined by a robust pro-

777 censing scheme), but not the original time series of the electromagnetic field  
 778 components. Hence, we cannot determine any error estimates ourselves or  
 779 to evaluate the reliability of the error estimates provided. When we perform  
 780 the inversions (both a single MT inversion and the adaptive joint inversion),  
 781 it is not possible to reach the proposed target misfits for MT even with fine  
 782 gridding. Dimensionality analysis indicates that the resistivity distribution  
 783 are either 1-D or 2-D (with the strike oriented perpendicular to the profile  
 784 direction), so 3-D effects can be largely excluded as the cause for high mis-  
 785 fits, which leads us to conclude that errors are generally underestimated.  
 786 We therefore choose for the joint inversion target misfits that are similar to  
 787 the minimum misfits we obtain from single MT inversions. During the joint  
 788 inversion we observe (see discussion below) that coupling parameters of the  
 789 MT are not extremely low for the chosen target misfit and that the results are  
 790 generally meaningful indicating that the chosen target misfit is appropriate.

#### 791 *4.2. Parameters used for the joint inversion*

792 The model consists of 68 and 71 inversions cells in x- and z-direction,  
 793 respectively, with a constant cell size of  $0.5 \times 0.1$  km. Starting models  
 794 for the gravity and MT inversion have constant densities and resistivities  
 795 of  $d = 2.5g/cm^3$  and  $\rho = 10\Omega m$  below a high conductive and low-density  
 796 layer associated with the seawater column of the ocean. The velocities of  
 797 the seismic starting model gradually increase with depth from  $1500m/s$  at  
 798 the sea-bottom to  $6000m/s$  at 4000 m depth. As for the synthetic tests,  
 799 the coupling strengths vary adaptively during the joint inversion procedure.  
 800 To control the convergence speed  $D^{seis.}$ ,  $D^{grav.}$  and  $D^{MT}$  of 0.4 are cho-  
 801 sen and  $\tilde{L} = 3$  iterations are used for each method to modify the  $\mu$ -value

802 for a subsequent iteration. The coupling parameters at the first iterations  
803 are set to  $\mu^{seis.} = \mu^{grav.} = \mu^{MT} = 0.25$ . The calculation of the projec-  
804 tion is governed by resolution estimates as already described above and the  
805 regularisation parameters  $\lambda$  are gradually reduced from starting values of  
806  $\lambda^{seis.} = \lambda^{grav.} = \lambda^{MT} = 0.25$  by using the method proposed by Lelièvre et al.  
807 (2012). Structural cross-coupling is only used for the last iterations ( $> 60$ ).

### 808 4.3. Joint inversion results

809 The convergence behaviour for all three methods (see Fig. 12) is stable  
810 and target misfits for gravity, seismic and MT are reached after 3, 13 and 60  
811 iterations, respectively. Similar observed data and calculated data from the  
812 joint inversion (see Figures 13, 14 and 15) indicate that the data are well-  
813 fitted for all methods. The final parameter models from this joint inversion  
814 run are shown in Fig. 16, Row 2. To evaluate the improvements obtained  
815 by using our joint inversion strategy, we perform corresponding separate  
816 inversion with similar parameters as for the joint inversion (same starting  
817 models, same inversion grid, similar regularization strength). It is obvious  
818 that the joint inversion results are more consistent with each other than  
819 the results from the individual inversions (compare Row 1 and Row 2 of  
820 Fig. 16). In the joint inversion models low  $v_p$ ,  $d$  and  $\rho$  values at shallow  
821 depths are separated by a sharp boundary from quasi horizontal high velocity,  
822 high density and high resistivity anomalies present in a depth range from  
823 about 2000 to 4000 m. Below 4000 m the physical parameters gradually  
824 decrease again with depth. These anomaly distributions are associated with  
825 a basaltic sequence enclosed by sediments above and below. In contrast,  
826 the single seismic inversion **resolves** only well the upper sediments and top

827 basalt, but no structures underneath. The single MT inversion creates a  
828 mostly horizontal high-resistive layer in the western and central part of the  
829 profile that is covered by MT stations. The anomaly is, however, too thick to  
830 realistically represent the basaltic sequence. The horizontal density anomaly  
831 from the single gravity inversion results is not well resolved and is largely  
832 dependent on the chosen starting model.



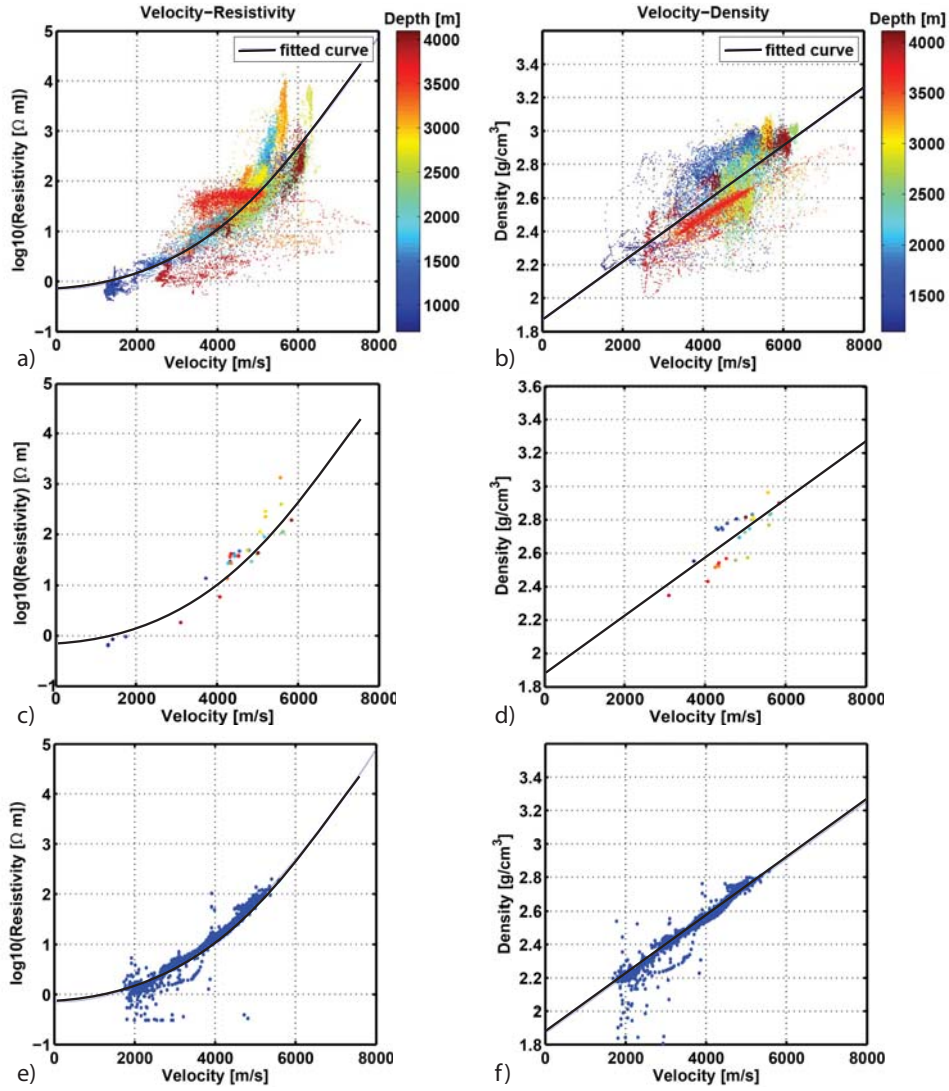


Figure 11: a) and b): Cross plots of the logging data from the borehole BRUGDAN. Color-coding of the dots is associated with the actual depths. c) and d): Mean values of physical properties calculated for 100 meter intervals and presented in the same form as for a) and b). e) and f): Cross plots for the final results of the adaptive joint inversion. Black lines show parameter relationships determined by fitting of logging data, which are used in our joint inversions.

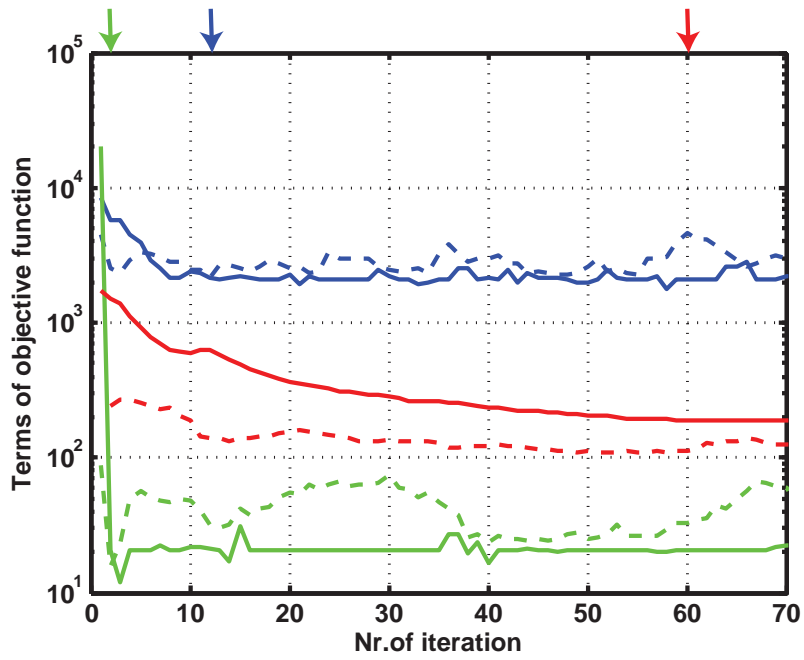


Figure 12: Convergence of our adaptive joint inversion for real data example. Values of data and regularization terms of the objective functions are plotted as continuous and dashed lines, respectively. Seismic data, gravity data and MT data are shown in blue, green and red, respectively. Arrows indicate iterations at which target misfits for the associated methods are reached.

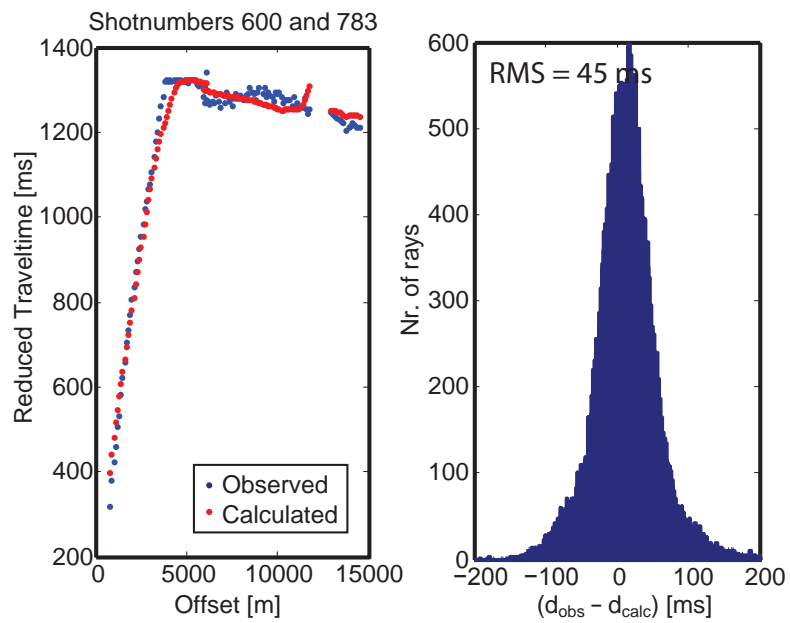


Figure 13: Final seismic data misfits for the adaptive joint inversion. Left: Picked first arrival times (red) for a typical shot gather together with the corresponding calculated traveltimes (blue). Traveltimes in the shot gather are reduced with a velocity of 5000 m/s, Right: Histogram of data misfits from all seismic first arrival times used in joint inversion.

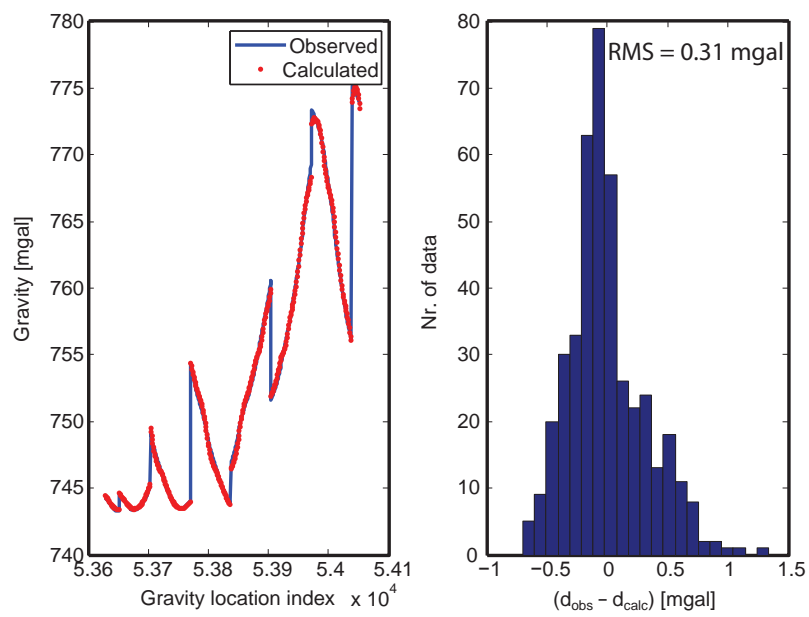


Figure 14: Final gravity data misfits for the adaptive joint inversion. Left: Observed (blue) and calculated (red) gravity responses for all measuring points. Right: Histogram of the gravity data misfits.

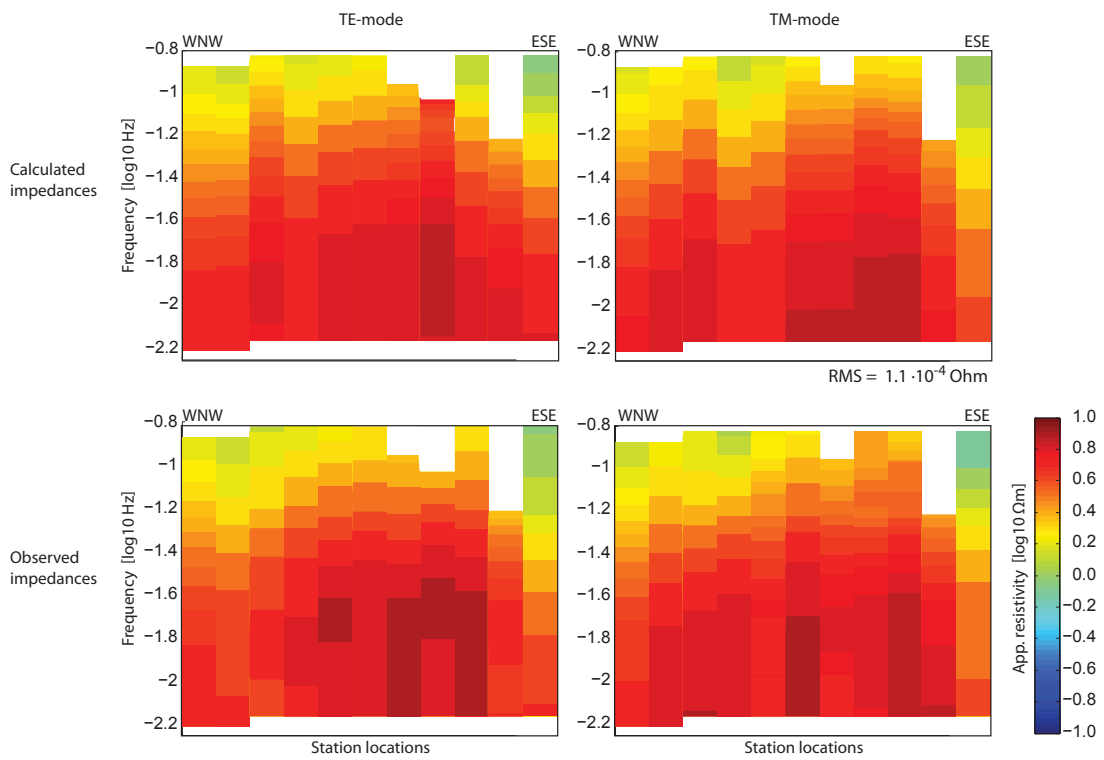


Figure 15: Final MT responses obtained from the adaptive joint inversion. Apparent resistivities for all frequencies and stations are shown for the calculated (top panels) and observed (bottom panels) responses for TE mode (left) and TM mode (right) polarization.

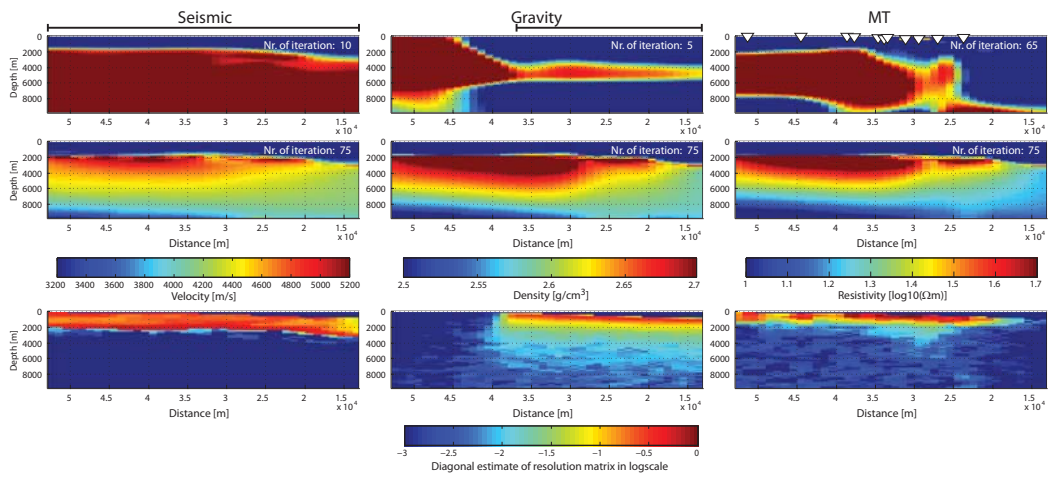


Figure 16: Inversion results and resolution estimates for the seismic, gravity and MT data used for the real data example. First and second row show the results from separate inversions and adaptive joint inversion. Black lines above the velocity model and density model indicate areas, where seismic and gravity data were acquired. Triangles above the resistivity model mark the positions of the marine MT sites. Third row shows approximations of the diagonal elements of the resolution matrices for the final models of the joint inversion (second row).

833 Although the results from joint inversion are consistent, the total reso-  
834 lution below the top basalt is relatively low for all methods (see diagonal  
835 estimates of the resolution matrices in Fig, 16, Row 3). Lack of measure-  
836 ment sites for gravity and MT at the west and east side of the profile result  
837 in a strongly reduced resolution in these areas. This indicates that a more  
838 complete coverage and the use of other data; e.g. seismic reflection onsets  
839 in the seismic (Fliedner and White, 2003) or CSEM (Panzner et al., 2014;  
840 Hoversten et al., 2015) could further improve the results particularly at larger  
841 depths.

842 As mentioned above the physical parameter relationships are only es-  
843 timates which are not valid everywhere and we indeed observe decoupling  
844 in some parts. Coupling parameters are with  $\mu^{seis.} = 0.0010 - 0.0227$  and  
845  $\mu^{MT} = 0.045 - 0.212$  low for seismic and MT at the late iterations (60 to 65)  
846 - only  $\mu^{grav.}$  has higher values ranging from 0.33 to 0.45, and cross-plots of  
847 the physical parameters of the final joint inversion results (Fig. 11e-f) show  
848 distinct deviations from the relationships for a number of inversion cells.

849 To verify our joint inversion results we compare the joint inversion mod-  
850 els with 3-D reflection seismic data and borehole data. Since the z-axis of  
851 the reflection seismic data set is given in time and not in depth, the final  
852 joint inversion models are converted to two-way travel-times by using the  
853 velocity model obtained from the joint inversion. In Figure 17 the resultant  
854 resistivity model is shown together with the cross-section of the 3-D seis-  
855 mic data cube along the FLA6 profile. Although both, resistivity and the  
856 seismic model, have some uncertainty, the top basalt reflection in the seis-  
857 mic data coincides well with the sharp boundary between low resistivities

858 associated with the shallow sediments and high resistivities associated with  
859 the basalt. It demonstrates that joint inversion provides accurate results  
860 in the well-resolved shallow part. Comparison in the deeper part is much  
861 more difficult because both reflection seismic and joint inversion give less  
862 clear results. A distinct seismic reflection associated with the base basalt  
863 is absent, but instead there is a pattern of discontinuous reflections that is  
864 interpreted as the base basalt (see dashed line in Fig. 17). The data from the  
865 bottom of the BRUGDAN borehole (Schuler et al., 2012) and results from  
866 wide-angle seismic studies (Fliedner and White, 2003; Spitzer et al., 2003)  
867 support this interpretation. Resolution of the joint inversion is significantly  
868 reduced at this depth range resulting in smooth changes in the parameter  
869 models. To evaluate if the thickness and, hence, the lower bound of the hor-  
870 izontal anomalies with large physical properties representing the basalt layer  
871 ( $v_p > 4500m/s$  and  $\rho > 30\Omega m$ ) are reliable, we repeat the joint inversion  
872 with different starting models. Results show that thicknesses of anomalies  
873 are generally stable for most of the western and the central part, but not in  
874 the eastern part which is not covered by MT sites. Comparison of the joint  
875 inversion models with the logging data as a function from depth shows that  
876 the modelled physical parameters are in the same range as the logging data  
877 for both the upper sediments and the basalt, however, variations within the  
878 basaltic sequence are not resolved (Fig. 10).

879 Other studies based on seismic data note that a NE-SW striking structural  
880 high of the pre-rifted basement - the East Faroe High - rises in the vicinity  
881 of the BRUGDAN borehole and the white arrows in Figure 17 may indicate  
882 reflections associated with this structure. However, in the joint inversion



883 model no such structure is observed, which we attribute to the fact that the  
884 resolution of the methods combined in the joint inversion is not high enough  
885 to resolve the deep basement.

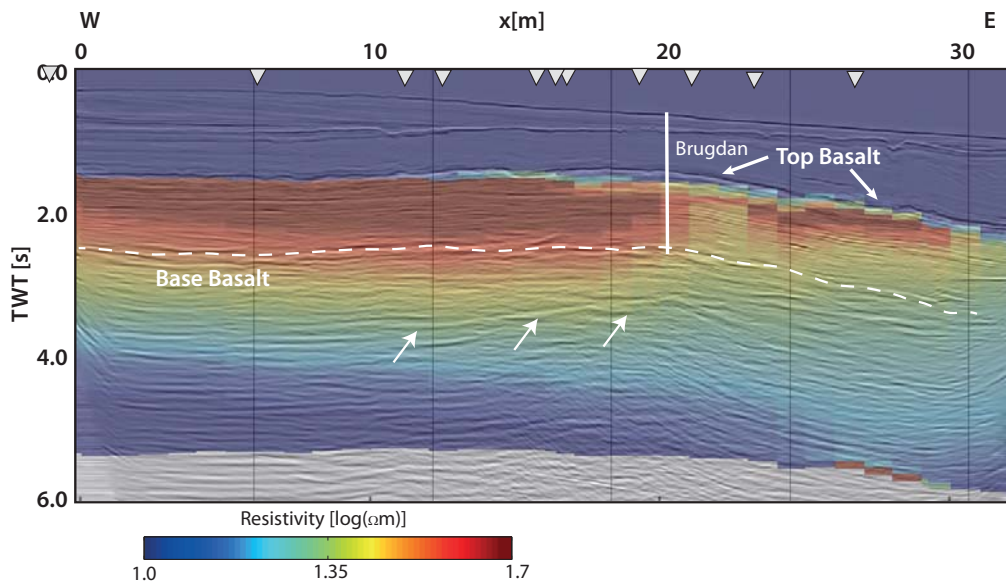


Figure 17: The transparent resistivity image from the joint inversion superimposes the cross-section from the 3-D reflection seismic dataset along the FLA6 profile (see Fig. 9). To transfer the depth axis of the resistivity image to two-way-travel times, the final velocity model from the joint inversion is used. Triangles indicate the locations of MT stations and dashed lines show the basalt as proposed by reflections seismic and logging data from the BRUGDAN borehole. Arrows highlight some reflectors associated with the pre-rifted basement.

## 886 5. Conclusion and Outlook

887 We have demonstrated that critical issues associated with joint inversion  
888 algorithms are handled in our joint inversion scheme: 1) a petrophysical joint  
889 inversion, in which parameter relationships are considered as constraints, re-  
890 quires no relative weighting of the data sets; 2) both for the synthetic tests  
891 and in the real data example, we observe that the implemented adaption  
892 of the coupling parameters makes the convergence of the individual meth-  
893 ods robust and independent of the choice of parameters controlling the joint  
894 inversion as the adaption rates  $D$ . For all runs with the adaptive joint inver-  
895 sion, the target misfits are reached for all methods and results are close to  
896 the true models; 3) by considering the spatially dependent resolution power  
897 of the individual methods in the coupling constraints, the convergence be-  
898 haviour is improved compared to the same joint inversion where resolution  
899 estimates are not incorporated; 4) results from the real data example show  
900 that the obtained rock property behaviour can deviate from the assumed pa-  
901 rameter relationships used as constraints. This happens when the true rock  
902 properties are, in parts, not adequately represented by the relationships and  
903 a too strong coupling is in disagreement with low data misfits.

904 In addition to these critical issues, we have shown that also structural in-  
905 formation can be easily incorporated in this otherwise petrophysically linked  
906 joint inversion scheme by adjusting the smoothing constraints by mutual  
907 cross-coupling. Such added structural information sharpens parameter bound-  
908 aries in parts of the models that are well resolved for some of the geophysical  
909 methods used.

910 Application of the adaptive joint inversion scheme on a combined wide-

911 angle seismic, MT and gravity data set that was acquired offshore the Faroe  
912 Islands, a region that is characterized by large-scaled flood basalt, demon-  
913 strates that this joint inversion works reliably also for real data and provides  
914 more consistent results than individual inversions. However, the same results  
915 indicate that even the combination of these methods is unable to adequately  
916 resolve deep structures such as thickness of the sub-basalt sediments and the  
917 pre-rifted basement. This is not directly related to our joint inversion strat-  
918 egy but to the low resolution power of the methods in the deeper subsurface.  
919 To resolve sub-basalt structures more complete coverage and possibly other  
920 geophysical data are required. For example we recommend to use reflection  
921 events in the seismic tomography and to add CSEM as another electromag-  
922 netic method (Panzner et al., 2014; Hoversten et al., 2015) in the future.

## 923 6. ACKNOWLEDGMENTS

924 We thank *Wintershall* and the *SINDRI* consortium for sponsoring the  
925 research position of Björn Heincke and part of this project (project num-  
926 ber C46-54-01). We thank Bernd Lahmeyer (*Statoil*, Stavanger), Christian  
927 Berndt (*GEOMAR*, Kiel) and an anonymous reviewer for helpful comments.  
928 David Bösing (*Baker&Hughes*, Celle) supported this work by evaluating dif-  
929 ferent resolution estimates. *Statoil* provided us the field data used in this  
930 study.

## 931 Appendix A. Projection method

932 Given a point  $P$ , consisting of the  $n$  physical parameters  $m^{(1)}, \dots, m^{(n)}$ , we  
933 use an iterative method to determine a projection  $\tilde{P} = (\tilde{m}^{(1)}, \dots, \tilde{m}^{(n)})$  onto a

934 pre-defined relationship curve. Convergence of this method is assured as long  
 935 as the relationship curve is strictly monotonic. Although only two physical  
 936 parameters are used in the following example (Fig. A.18), we emphasize that  
 937 the method is in general not limited by the number of considered physical  
 938 parameters.

939 In the first iteration of the procedure, lines parallel to the  $x$ - and  $y$ -axis  
 940 that pass through the point  $P = (m^{(1)}, m^{(2)})$  are determined (Fig. A.18a).  
 941 For these lines, the points of intersection  $A = (m_{A,1}^{(1)}, m_{A,1}^{(2)})$  and  $B = (m_{B,1}^{(1)}, m_{B,1}^{(2)})$   
 942 with the relationship curve are determined and the mean values  $m_{AB,1}^{(1)} =$   
 943  $\frac{m_{A,1}^{(1)} + m_{B,1}^{(1)}}{2}$  and  $m_{AB,1}^{(2)} = \frac{m_{A,1}^{(2)} + m_{B,1}^{(2)}}{2}$  are calculated. For the next iteration  
 944 axis parallel lines passing through  $m_{AB,1}^{(1)}$  and  $m_{AB,1}^{(2)}$  are then used to de-  
 945 termine new points of intersection with the relationship curve  $(m_{A,2}^{(1)}, m_{A,2}^{(2)})$   
 946 and  $(m_{B,2}^{(1)}, m_{B,2}^{(2)})$  (Fig. A.18b). From these points again the mean values  
 947  $m_{AB,2}^{(1)} = \frac{m_{A,2}^{(1)} + m_{B,2}^{(1)}}{2}$  and  $m_{AB,2}^{(2)} = \frac{m_{A,2}^{(2)} + m_{B,2}^{(2)}}{2}$  are determined.

948 At every iteration the two points of intersection converge against each  
 949 other. If the distance between the intersections points becomes smaller than  
 950 a pre-defined threshold value at the  $t$ -th iteration the procedure is stopped.  
 951 The mean values of the points of intersection  $(\frac{m_{A,t}^{(1)} + m_{B,t}^{(1)}}{2}, \frac{m_{A,t}^{(2)} + m_{B,t}^{(2)}}{2})$  is then  
 952 considered as the projection point  $\tilde{P} = (\tilde{m}^{(1)}, \tilde{m}^{(2)})$ .

953 Because  $m_{AB}^{(1)}$  and  $m_{AB}^{(2)}$  depend on variations of the first and second phys-  
 954 ical parameter, respectively, the influence of the different parameters is in-  
 955 herently balanced and, hence, more or less independent of employed units  
 956 and slope of the relationship curve.

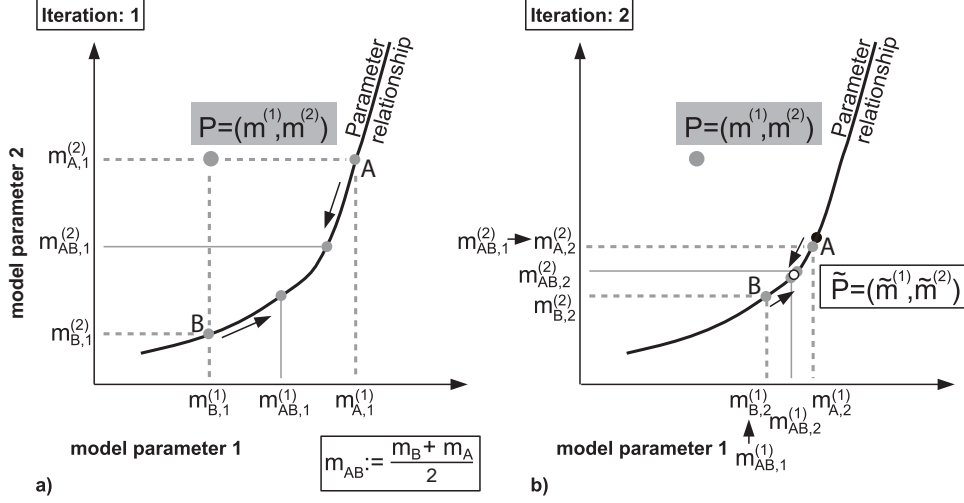


Figure A.18: Sketch illustrating the iterative procedure to determine for a point of two physical parameters  $m^{(1)}$  and  $m^{(2)}$  a projection  $(\tilde{m}^{(1)}, \tilde{m}^{(2)})$  onto a relationship curve. (a) and (b) show the 1st and 2nd iteration step of the procedure assuming that both parameters are equally weighted. The white and black dot in b) show the obtained projection point if the same weights and different weights of  $\psi = 1.0$  and  $\phi = 0.5$  are considered for the two parameters (see Appendix B), respectively.

957 **Appendix B. Modification of the projection to account for the**  
 958 **model resolutions**

959 The general procedure is the same as already described as in the Appendix  
 960 A. However, the sums  $m_{AB,t}^{(1)}$  and  $m_{AB,t}^{(2)}$  are now calculated by some weighted  
 961 mean values. In the case of having two parameters and using the diagonal  
 962 elements  $d^{(1)}$  and  $d^{(2)}$  of the resolution matrix as measures, they are obtained  
 963 as:

$$\begin{aligned}
m_{AB,t}^{(1)} &= \frac{\psi m_{A,t}^{(1)} + \phi m_{B,t}^{(1)}}{|\psi| + |\phi|} \\
m_{AB,t}^{(2)} &= \frac{\psi m_{A,t}^{(2)} + \phi m_{B,t}^{(2)}}{|\psi| + |\phi|} \\
\text{with } \psi &= 1.0 - |1.0 - d^{(1)}| \quad \text{if } \gamma \leq d^{(1)} \leq 2.0 \\
&\psi = \gamma \quad \text{otherwise} \\
\text{with } \phi &= 1.0 - |1.0 - d^{(2)}| \quad \text{if } \gamma \leq d^{(2)} \leq 2.0 \\
&\phi = \gamma \quad \text{otherwise}
\end{aligned}$$

964  $\gamma$  is a small positive value (we use in all test  $\gamma = 0.002$ ) that is intro-  
965 duced to make the determination of the projection direction less sensitive  
966 to inaccurate calculation of the diagonal element estimates of the resolution  
967 matrix.

968 The black dot in Figure A.18b shows the projection point for weights of  
969  $\psi = 1.0$  and  $\phi = 0.5$ .

## 970 References

- 971 M. Moorkamp, P. Lelievre, N. Linde, A. Khan (Eds.), Integrated Imaging of  
972 the Earth, AGU-Wiley, 2016.
- 973 P. Xu, Iterative generalized cross-validation for fusing heteroscedastic data  
974 of inverse ill-posed problems, *Geophys J. Int.* 179 (2009) 182–200.
- 975 A. Abubakar, M. Li, J. Liu, T. Habashy, Simultaneous joint inversion of MT  
976 and CSEM data using a multiplicative cost-function, in: SEG Technical  
977 Program Expanded Abstracts, Houston, USA, vol. 29, 719–723, 2009.

- 978 T. Günther, C. Rücker, A new joint inversion approach applied to the com-  
979 bined tomography of DC resistivity and seismic refraction data., in: Ex-  
980 panded Abstract for 19. EEGS annual meeting (SAGEEP), Seattle, USA,  
981 2006.
- 982 H. Paasche, J. Tronicke, Cooperative inversion of 2D geophysical data sets:  
983 A zonal approach based on fuzzy c-means cluster analysis, *Geophysics* 72  
984 (2007) A35–A39.
- 985 A. Bouchedda, M. Chouteau, A. Binley, B. Giroux, 2-D joint inversion of  
986 cross-hole electrical resistance and ground penetrating radar data, *Journal*  
987 *of Applied Geophysics* 78 (2012) 52–67.
- 988 T. Zhu, J. M. Harris, Improved estimation of P-wave velocity, S-wave velocity,  
989 and attenuation factor by iterative structural joint inversion of crosswell  
990 seismic data, *Journal of Applied Geophysics* 123 (2015) 71 –80.
- 991 M. E. Kilmer, D. P. O’Leary, Choosing regularization parameters in iterative  
992 methods for ill-posed problems, *SIAM J. Matrix Anal. Appl.* 22 (2001)  
993 1204–1221.
- 994 C. R. Vogel, *Computational Methods for Inverse Problems*, *Frontiers in ap-*  
995 *plied mathematics*. Society for Industrial and Applied Mathematics, 2002.
- 996 P. C. Hansen, Analysis of discrete ill-posed problems by means of the L-curve,  
997 *SIAM Review* 34 (1993) 561–580.
- 998 G. H. Golub, C. F. Van Loan, *Matrix Computations*, John Hopkins Univer-  
999 sity Press, Baltimore, 3 edn., 1996.

- 1000 V. A. Morozov, On the solution of functional equations by the method of  
1001 regularization, *Soviet mathematics - Doklady* 7 (1966) 414 – 417.
- 1002 P. G. Lelièvre, C. G. Farquharson, C. A. Hurich, Joint inversion of seismic  
1003 traveltimes and gravity data on unstructured grids with application to  
1004 mineral exploration, *Geophysics* 77 (2012) K1–K15.
- 1005 L. A. Gallardo, M. A. Meju, Joint two-dimensional DC resistivity and seis-  
1006 mic travel time inversion inversion with cross-gradients cross constraints,  
1007 *Journal of Geophysical Research* 109 (2004) B03311.
- 1008 L. A. Gallardo, Multiple cross-gradient joint inversion for geospectral imag-  
1009 ing, *Geophysical Research Letters* 34 (2007) L19301.
- 1010 M. Lien, Simultaneous joint inversion of amplitude-versus-offset and  
1011 controlled-source electromagnetic data by implicit representation of com-  
1012 mon parameter structure, *Geophysics* 78 (2013) ID15–ID27.
- 1013 E. Haber, D. Oldenburg, Joint inversion: a structural approach, *Inverse Prob-  
1014 lems* 13 (1997) 63–77.
- 1015 J. Doetsch, N. Linde, A. Binley, Structural joint inversion of time-lapse  
1016 crosshole ERT and GPR traveltime data, *Geophysical Research Letters*  
1017 37 (2010) L24404.
- 1018 D. M. Molodtsov, V. N. Troyan, Y. V. Roslov, A. Zerilli, Joint inversion  
1019 of seismic traveltimes and magnetotelluric data with a directed structural  
1020 constraint, *Geophysical Prospecting* 61 (2013) 1218–1228.



- 1021 M. Moorkamp, A. W. Roberts, M. Jegen, B. Heincke, R. W. Hobbs, Verifi-  
1022 cation of velocity-resistivity relationships derived from structural joint in-  
1023 version with borehole data, *Geophysical Research Letters* 40 (2013) 3596–  
1024 3601.
- 1025 J. M. Lees, J. C. VanDecar, Seismic tomography constrained Bouguer gravity  
1026 anomalies: Applications in western Washington, *Pure and Applied Geo-*  
1027 *physics* 135 (1991) 31–52.
- 1028 Afnimar, K. Koktsu, K. Nakagawa, Joint inversion of refraction and gravity  
1029 data for the three-dimensional topography of a sediment-basement inter-  
1030 face, *Geophysical Journal International* 151 (2002) 243–254.
- 1031 M. Moorkamp, B. Heincke, M. Jegen, A. W. Roberts, R. W. Hobbs, A frame-  
1032 work for 3-D joint inversion of MT, gravity and seismic refraction data,  
1033 *Geophysical Journal International* 184 (2011) 477–493.
- 1034 D. Colombo, M. D. Stefano, Geophysical modeling via simultaneous joint  
1035 inversion of seismic, gravity, and electromagnetic data: Application to  
1036 prestack depth imaging, *The Leading Edge* (2007) 326–331.
- 1037 P. G. Lelièvre, C. G. Farquharson, C. A. Hurich, Joint inversion of seis-  
1038 mic traveltimes and gravity data on unstructured grids with applications  
1039 to mineral exploration, in: *SEG Technical Program Expanded Abstracts*,  
1040 Denver, USA, vol. 25, 1758–1762, 2010.
- 1041 L. Nielsen, B. H. Jacobsen, Integrated gravity and wide-angle seismic inver-  
1042 sion for two-dimensional crustal modelling, *Geophysical Journal Interna-*  
1043 *tional* 140 (2000) 222–232.

- 1044 G. M. Hoversten, F. Cassassuce, E. Gasperikova, G. A. Newman, J. Chen,  
1045 Y. Rubin, Z. Hou, D. Vasco, Direct reservoir parameter estimation using  
1046 joint inversion of marine seismic AVA and CSEM data, *Geophysics* 71  
1047 (2006) C1–C13.
- 1048 P. Dell’Aversana, G. Beransconi, F. Miotti, D. Rovetta, Joint inversion of  
1049 rock properties from sonic, resistivity and density well-log measurements,  
1050 *Geophysical Prospecting* 59 (2011) 1144–1154.
- 1051 N. Juhojuntti, J. Kamm, Joint inversion of seismic refraction and resistivity  
1052 data using layered models - Applications to groundwater investigations,  
1053 *Geophysics* 80 (2015) EN43–EN55.
- 1054 J. Sun, Y. Li, A general framework for joint inversion with petrophysical in-  
1055 formation as constraints, in: *SEG Technical Program Expanded Abstracts*,  
1056 Houston, USA, 2013.
- 1057 P. Podvin, I. Lecomte, Finite-difference computation of traveltimes in very  
1058 contrasted velocity models: A massively approach and its associated tools,  
1059 *Geophysical Journal International* 105 (1991) 271–284.
- 1060 D. F. Aldridge, D. W. Oldenburg, Two-dimensional inversion with finite-  
1061 difference traveltimes, *Journal of Seismic Exploration* 2 (1993) 257–274.
- 1062 G. W. Bear, H. J. Al-Shukri, A. J. Rudman, Linear inversion of gravity data  
1063 for 3-D density distributions, *Geophysics* 60 (1995) 1354–1364.
- 1064 P. E. Wannamaker, J. A. Stodt, L. Rijo, A stable finite element solution for  
1065 two-dimensional magnetotelluric modelling, *Geophys. J. R. astr. Soc.* 88  
1066 (1987) 277–296.

- 1067 J. Nocedal, S. Wright, Numerical Optimization, Springer, second edition  
1068 edn., 2006.
- 1069 C. C. Paige, M. A. Saunders, LSQR: An Algorithm for Sparse Linear Equa-  
1070 tions and Sparse Least Squares, ACM Transactions on Mathematical Soft-  
1071 ware 8.
- 1072 C. J. Ammon, J. E. Vidale, Tomography without rays, Bulletin of the Seis-  
1073 mological Society of America 83 (1993) 509–528.
- 1074 J. J. Moré, D. Thüente, Line search algorithms with guaranteed sufficient  
1075 decrease, ACM Transactions on Mathematical Software 20 (1994) 286–  
1076 307.
- 1077 J. MacCarthy, B. Borchers, R. Aster, Efficient stochastic estimation of the  
1078 model resolution matrix diagonal and generalized cross-validation for large  
1079 geophysical inverse problems., Journal of Geophysical Research 116 (2011)  
1080 B10304.
- 1081 C. Bekas, E. Kokiopoulou, Y. Saad, An estimator for the diagonal of a matrix,  
1082 Applied Numerical Mathematics 57 (2007) 1214 – 1229.
- 1083 S. Constable, R. Parker, C. Constable, Occam’s inversion: a practical algo-  
1084 rithm for generating smooth models from electromagnetic sounding data,  
1085 Geophysics 52 (1987) 289–300.
- 1086 C. de Groot-Hedlin, S. Constable, Occam’s inversion to generate smooth,  
1087 two-dimensional models for magnetotelluric data, Geophysics 55 (1990)  
1088 1613–1624.

- 1089 F. Martini, R. Hobbs, C. Bean, R. Single, A complex 3D volume for sub-  
1090 basalt imaging, *first break* 23 (2005) 41–51.
- 1091 G. W. Purnell, Imaging beneath a high-velocity layer using converted waves,  
1092 *Geophysics* 57 (1992) 1444–1452.
- 1093 M. M. Flidner, R. S. White, Depth imaging of basalt flows in the Faeroe-  
1094 Shetland Basin, *Geophysical Journal International* 152 (2003) 353–371.
- 1095 S. Hautot, R. T. Single, J. Watson, N. Harrop, D. A. Jerram, P. Tarits,  
1096 K. Whaler, G. Dawes, 3-D magnetotelluric inversion and model valida-  
1097 tion with gravity data for the investigation of flood basalts and associ-  
1098 ated volcanic rifted margins, *Geophysical Journal International* 170 (2007)  
1099 1418–1430.
- 1100 M. Panzner, W. W. Weibull, J. P. Morten, Sub-basalt imaging in the Faroe-  
1101 Shetland Basin using CSEM&MT data to constrain the velocity model, in:  
1102 SEG Technical Program Expanded Abstracts, Denver, USA, 2014.
- 1103 G. Hoversten, D. Myer, K. Key, D. Alumbaugh, O. Hermann, R. Hobbet,  
1104 Field test of sub-basalt hydrocarbon exploration with marine controlled  
1105 source electromagnetic and magnetotelluric data, *Geophysical Prospecting*  
1106 63 (2015) 1284–1310.
- 1107 B. Heincke, M. Jegen, R. W. Hobbs, Joint inversion of MT, gravity and  
1108 seismic data applied to sub-basalt imaging, in: SEG Technical Program  
1109 Expanded Abstracts, New Orleans, USA, vol. 25, 784–789, 2006.
- 1110 D. Colombo, M. Mantovani, S. Hallinan, M. Virgilio, Sub-basalt depth imag-  
1111 ing using simultaneous joint inversion of seismic and electromagnetic (MT)

- 1112 data: a CRB field study, in: SEG Technical Program Expanded Abstracts,  
1113 Las Vegas, USA, vol. 27, 2674–2678, 2008.
- 1114 A. Manglik, S. K. Verma, K. H. Singh, Detection of sub-basaltic sediments  
1115 by a multi-parametric joint inversion approach, *Journal of Earth System*  
1116 *Science* 118 (2009) 551–562.
- 1117 M. D. Jegen, R. W. Hobbs, P. Tarits, A. Chave, Joint inversion of ma-  
1118 rine magnetotelluric and gravity data incorporating seismic constraints:  
1119 Preliminary results of sub-basalt imaging off the Faroe Shelf, *Earth and*  
1120 *Planetary Science Letters* 282 (2009) 47–55.
- 1121 P. Tarits, *Algorithme de modlisation magntotelluric en deux dimension*,  
1122 Ph.D. thesis, IPG, Paris, France, 1984.
- 1123 R. S. White, J. R. Smallwood, M. M. Fliedner, B. Boslaugh, J. Maresh,  
1124 J. Fruehn, Imaging and regional distribution of basalt flows in the Faroe-  
1125 Shetland Basin, *Geophysical Prospecting* 51 (2003) 215–231.
- 1126 J. Gallagher, P. Dromgoole, Exploring below the basalt, offshore Faeroes: a  
1127 case history of sub-basalt imaging, *Petroleum Geoscience* 13 (2007) 213–  
1128 225.
- 1129 J. Schuler, P. A. F. Christie, R. S. White, Seismic Attenuation of Flood  
1130 Basalts in the Brugdan and William Wells and stratigraphic Correlation  
1131 on the Faeroe Shelf, EAGE 74th Conference & Exhibition, Copenhagen,  
1132 Denmark .

1133 O. Dubrule, Geostatistics for seismic data integration in earth models, Dis-  
1134 tinguished Instructor Series No.6., EAGE, Distinguished Instructor Series  
1135 No.6., 2003.

1136 R. Spitzer, R. S. White, P. A. F. Christie, Enhancing subbasalt reflections  
1137 using parabolic Tau-p transformation, The Leading Edge (2003) 1184 –  
1138 1201.